Accepted Manuscript

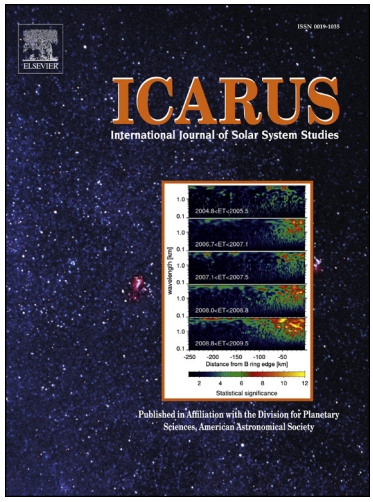

Impact of lightning on the lower ionosphere of Saturn and possible generation of halos and sprites

D. Dubrovin, A. Luque, F.J. Gordillo-Vazquez, Y. Yair, F.C. Parra-Rojas, U. Ebert, C. Price

PII: S0019-1035(14)00345-5
DOI: http://dx.doi.org/10.1016/j.icarus.2014.06.025
Reference: YICAR 11156

To appear in: *Icarus*

Received Date: 22 December 2013
Revised Date: 18 June 2014
Accepted Date: 24 June 2014

Please cite this article as: Dubrovin, D., Luque, A., Gordillo-Vazquez, F.J., Yair, Y., Parra-Rojas, F.C., Ebert, U., Price, C., Impact of lightning on the lower ionosphere of Saturn and possible generation of halos and sprites, *Icarus* (2014), doi: http://dx.doi.org/10.1016/j.icarus.2014.06.025

This is a PDF file of an unedited manuscript that has been accepted for publication. As a service to our customers we are providing this early version of the manuscript. The manuscript will undergo copyediting, typesetting, and review of the resulting proof before it is published in its final form. Please note that during the production process errors may be discovered which could affect the content, and all legal disclaimers that apply to the journal pertain.

ACCEPTED MANUSCRIPT

Impact of lightning on the lower ionosphere of Saturn and possible generation of halos and sprites

D. Dubrovin (1), A. Luque (2), F. J. Gordillo-Vazquez (2), Y. Yair (3)

F. C. Parra-Rojas (2), U. Ebert (4), C. Price (1)

(1) Department of Geophysical, Atmospheric and Planetary Sciences, Tel-Aviv University, Israel,

(2) Institute for Astrophysics of Andalusia (IAA-CSIC), Granada, Spain,

(3) Department of Life and Natural Sciences, The Open University of Israel, Ra'anana, Israel.

(4) Centrum Wiskunde & Informatica (CWI), Amsterdam, The Netherlands,

Revision

02/06/2014

Abstract

We study the effect of lightning on the lower ionosphere of Saturn. A self-consistent one-dimensional model of the electric field and electron density is used to estimate the changes of the local electron and photon emissions. The chemical fingerprint and ion densities are determined using a detailed self-consistent kinetic model. Charge moment change, depth of lightning flashes and their duration are estimated based on the known

ACCEPTED MANUSCRIPT

constraints of Saturnian lightning activity. We test two electron density profiles and find that the conservative estimation of lightning charge moment change 10^4 to 10^5 C km could lead to faint halos and possibly sprites if the base of the ionosphere is located at 1000 km above the 1 bar level; if the base of the ionosphere is located at 600 km then only the extreme scenario of a 10^6 C km charge moment change could induce considerable ionization, halos and possibly sprites. We found that H_3^+ ions are rapidly produced from the parent H_2^+ ions through the fast reaction $H_2^+ + H_2 \rightarrow H_3^+ + H$, so that H_3^+ becomes the dominant ion in all the scenarios considered. The resulting light emissions, mostly in the blue and ultraviolet spectral regions, are below the detection threshold of Cassini.

Keywords: Saturn, lightning, ionosphere, sprites, halos

1. Introduction

Lightning has been observed on several planets in the Solar system, and indirectly inferred on others (most recently reviewed in Yair (2012)). On the gas giants Jupiter and Saturn lightning activity is concentrated in thunderstorms with large physical dimensions, which exhibit vigorous convection and associated cloud systems. The existence of lightning flashes on Saturn was inferred from multiple observations of high frequency radio signals, known as Saturn Electrostatic Discharges (SED) (see review by Fischer et al. (2008)), as well as from optical observations by the Cassini spacecraft (Dyudina et al. ,2010, 2013). The most recent storm on Saturn, which started early December 2010 and lasted almost a year, was exceptionally active (Fischer et al. (2011); Dyudina et al. (2013)); lightning activity persisted for 9 months (Sayanagi et al. 2013). Lightning storms on Saturn are rare and are found at specific latitudes, many of them around 35

ACCEPTED MANUSCRIPT

degrees in both hemispheres. They typically occur in the respective hemisphere's summer.

Lightning activity on Earth is accompanied by transient luminous events (TLE) in the mesosphere above the thunderclouds (Pasko et al. (2012). TLE is an inclusive term which describes the electric breakdown in the mesosphere induced by a quasi-electrostatic field (sprites and halos), and the illumination of the lower ionosphere by the lightning electro-magnetic pulse (elves), as well as other phenomena. In this paper our focus is the quasi-electrostatic discharges that may include a visible diffuse region (a halo) and a lower filamentary region, which is commonly known as sprite. Our analysis deals with the formation of halos and sprites.

Sprites are observed mainly at night-time in the altitude range of 40 to 90 km, below the ionosphere. According to the commonly accepted model of sprite formation on Earth, they form as a result of the quasi-electrostatic field (QES) due to a charge moment change (CMC) in the thundercloud. The induced electric field will cause rapid growth in the electron density if it is strong enough. Eventually the electric field will be screened by the free electrons, and the process will stop. This process is accompanied by the excitation of molecules and optical emissions, perceived as an upward propagating visible halo, a diffuse brightening of Earth's upper mesosphere. The chemical influence of halos in the upper atmosphere of the Earth between 50 km and 85 km has been recently modeled by Parra-Rojas et al. (2013) . The halo is sometimes followed by bright tendrils at lower altitudes, similar to streamer discharges at standard pressure. For a comprehensive review of TLE physics and their chemical effects we refer the reader to Pasko et al. (2012).

The existence of powerful lightning discharges in other planetary atmospheres led Yair et al. (2009) to examine whether sprites can form in extra-terrestrial atmospheres, by analogy with the processes occurring on Earth. The conventional view on the occurrence

ACCEPTED MANUSCRIPT

conditions of discharges above terrestrial thunderclouds goes back to Wilson (1925). While the ionosphere is highly conducting and therefore rapidly screens the suddenly changing electric field above a lightning stroke, the electric field can exceed the classical break-down field in the low conductivity region of the night time terrestrial mesosphere, creating electric breakdown, in the form of halos and sprites. Yair et al. (2009) compared the electric field induced by various charge configurations with the local conventional breakdown field E_k, as calculated by Sentman (2004) for the respective atmospheric compositions. This approach, however, neglects the finite conductivity in the weakly ionized atmosphere below the ionosphere.

In this paper we examine the response of Saturn's ionosphere to the lightning flashes in the water-ice clouds. The paper is organized as follows: In section 2 we describe the known constraints on the lightning discharge, and derive possible CMC values and flash duration. In section 3 we discuss the electron density at the bottom side of Saturn's ionosphere. In section 4 we examine the response of the atmosphere at various altitudes to an externally applied electric field, taking the local conductivity into account. We find that $E>E_k$ is not always a sufficient criterion to predict whether the local electron density is affected. In section 5 the self-consistent zero-dimensional model of Luque and Gordillo-Vázquez (2011) is used to estimate the change in electron density due to the flash, and the optical features of the event. In section 6 a detailed self-consistent kinetic model of the reactions taking place in the perturbed Saturnian atmosphere (Gordillo-Vázquez (2008, 2010)) is used to estimate the chemical fingerprint and optical emissions of the event.

ACCEPTED MANUSCRIPT

2. Lightning on Saturn

2.1. Lightning Energy

The simulation of TLEs on Saturn requires some assumptions concerning the electric field applied by the lightning flash. We need to know the amount of charge neutralized by the lightning flash, and the duration of the stroke. The average total energy dissipated by a lightning discharge is estimated at 10^{12} to 10^{13} J, based on SED and optical observations (Fischer et al. (2007, 2006); Dyudina et al. (2010, 2013)). According to Dyudina et al. (2010) the observed lightning flashes are three orders of magnitude stronger than the median terrestrial lightning and comparable with terrestrial super-bolts. In Fischer et al. (2006) and elsewhere it was assumed that the duration of the lightning discharge is similar to Earth's intra-cloud (IC) discharges, several 10-s of microseconds (values for terrestrial lightning can be found in (Uman, 2001, p. 124)). Farrell et al. (2007) suggested that a faster discharge (~ 1 μs) would fit the observed SED frequency spectrum better, implying significantly lower energies (~ 10^9 J), comparable with typical terrestrial lightning energies. The optical observations by Dyudina et al. (2010, 2013) provide an independent confirmation of the high energy super-bolt like scenario (G. Fischer, personal communication).

2.2. Lightning current and electric field

In this work we follow the high energy scenario suggested by Fischer et al. (2006) and described by Farrell et al. (2007), where the current flowing through the lightning channel follows a bi-exponential function of the form

$$I(t) = I_0(\exp(-t/\tau_1) - \exp(-t/\tau_2)), \quad (1)$$

ACCEPTED MANUSCRIPT

where τ_2 represents the rise time of the current wave, and is typically 10 times faster than the overall duration of the stroke, represented by τ_1.

The lightning flash is located almost 1000 km below the region of interest (the lower ionosphere between 400 and 900 km above the 1 bar level). At these length scales the full electric field has to be considered. At small angles relative to a vertically oriented dipole-like discharge the vertical component of the electric field E_p is dominated by the quasi-electrostatic (QES) and the induction fields (Bruce and Golde, 1941),

$$E_p(z,t) = \frac{1}{\pi\epsilon_0}\left(\frac{1}{(z-z_p)^3}M\left(t-(z-z_p)/c\right) + \frac{1}{c(z-z_p)^2}\frac{d}{dt}M\left(t-(z-z_p)/c\right)\right) \quad (2)$$

where $M(t)$ is the charge moment change, z is the altitude where the field is measured and z_p is the altitude of the center of the dipole, ϵ_0 is the permittivity of vacuum, and c is the speed of light. The two terms in eq. (2) are the QES field and the induction field, respectively. The far field (EMP) component can be neglected at small angles. While the QES component dominates the electric field above the lightning flash on Earth, justifying the commonly used QES heating model of sprites, we find that on Saturn the induction component dominates. An example of the induced electric field on Saturn and on Earth is plotted in Figure 1.

The induction component of the field rises and decays with the current, eq. (1), reaching a maximum value on the time scale of the current rise time τ_2; the QES component reaches a constant value M/z^3 after the current has decayed, on the time scale of the flash duration τ_1, and then decays on the time scale of the local Maxwell relaxation time, as will be discussed in section 4. The induction component is stronger than the QES component, and it is applied faster, as a result it may significantly increase the local electron density, decreasing the local Maxwell time and causing very fast screening of the

ACCEPTED MANUSCRIPT

QES component. This happens if the characteristic ionization time is shorter than the duration of the induction field, so that the induction field has enough time to considerably increase the electron density. This point is discussed further in Section 4.

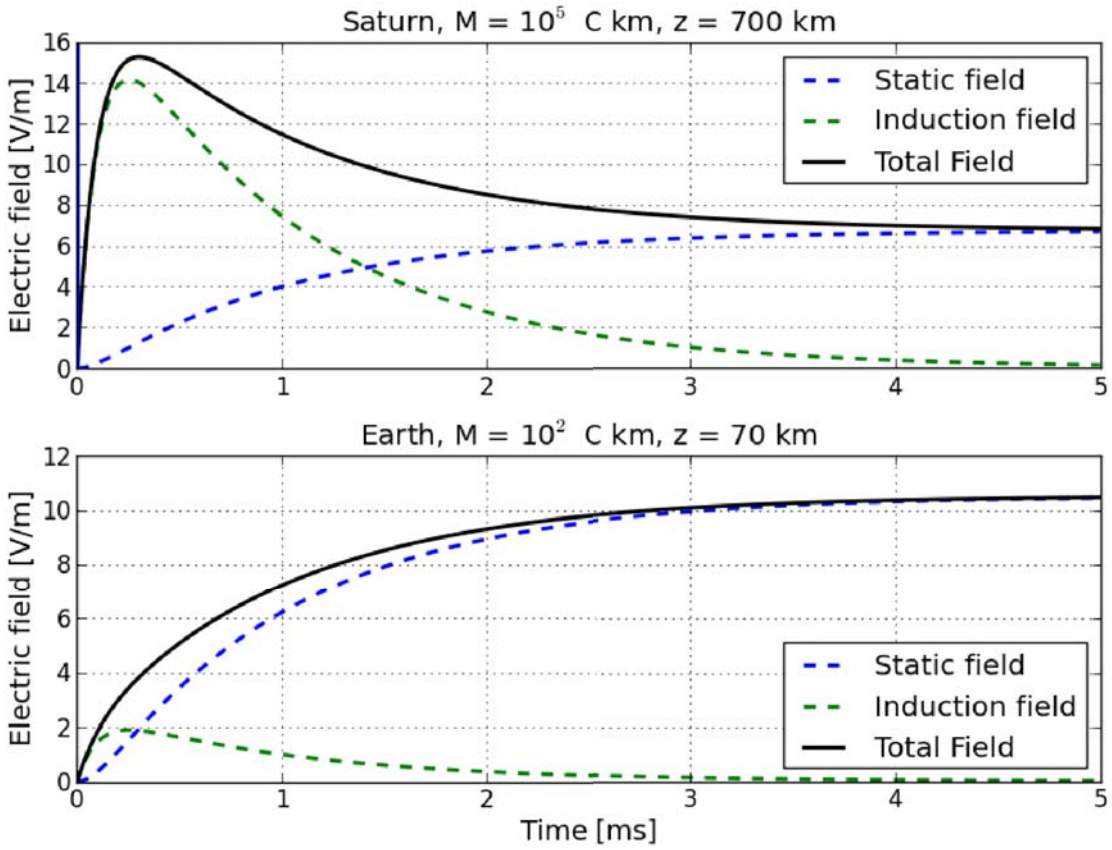

Figure 1: Top: The time evolution of the applied electric field at 700 km above the 1 bar level due to a stroke with a charge moment change of M=10^5 C km located at -110 km below the 1 bar level. The current follows eq. (1). The static (blue) and induction (green) components, and the total electric field (black), are calculated according to eq (2). The induction field reaches its maximum before the static field does, and then decays. Bottom: The applied electric field due to a cloud to ground flash on Earth induced by a charge moment change of M=10^2 C km, calculated at 70 km above ground. The center of the dipole is at 0 km. The induction component is weaker than the static component.

ACCEPTED MANUSCRIPT

2.3. Charge separation and charge moment change

The charge moment change (CMC) is commonly defined for terrestrial lightning as the product of the amount of charge and the height from which it was lowered to the ground (e.g. Bruce and Golde (1941)). On Saturn we define $M(t) = Q(t)a/2$, where a is the vertical separation of the charge cell centers, and $Q(t) = \int_0^t I(t')dt'$. The current $I(t)$ is defined in equation (1) above.

The storm clouds on Saturn are larger than on Earth, towering more than a hundred kilometers. However we do not know what is the extent of the charge separation. Yair et al. (1995) modeled the charging process in clouds on Jupiter and found that the charge separation corresponds with a lightning channel of 20 km. They also found that updraft in the developing stage is ~ 50 m/s. The clouds on Saturn are larger than on Jupiter, with stronger updrafts (~ 150 m/s, Sánchez-Lavega et al. (2011)), therefore we can assume that a lightning channel on Saturn spans larger vertical distances, starting from a few tens and up to a hundred kilometers. The typical return stroke propagation speed on Earth is 0.3 of the speed of light, therefore for a 100 km channel the stroke cannot be shorter than 1 ms. Therefore we set τ_1 = 1 ms and τ_2 = 0.1 ms. This means that the electric field in the mesosphere reaches its maximum within 1 ms. If the stroke duration is longer than the local relaxation time, the induced electric field at that altitude would be partially screened before it reached its maximum value, and a sprite is less likely.

We estimate the value of the CMC of Saturn's lightning based on the energy constraints and the physical size of the water ice clouds, assumed to be the lightning source in its atmosphere. The base of these clouds is located at 8 to 10 bar, 130 to 160 km below the 1 bar level (Atreya (1986); Atreya and Wong (2005)). During lightning-producing storms the cloud undergoes significant upward development, according to Sánchez-Lavega et al. (2011), reaching as high as the 0.1 bar level, ~ 90 km above the

ACCEPTED MANUSCRIPT

1 bar level. Strong updrafts in the cloud are estimated by Sánchez-Lavega et al. (2011) to reach 150 m/sec. Optical observations by Dyudina et al. (2010) and Dyudina et al. (2013) show a circular footprint of the lightning discharge at cloud-top, which allows to locate a point-like light source 125-250 km below the cloud top, within the water ice clouds. Dyudina et al. (2013) observed lightning flashes on the day-side. In these observations the cloud tops are estimated to be deeper than 1.2 bar.

A vertical channel acts as a multiple point source located at a range of altitudes. Therefore we suggest that for a vertically extended lightning channel the estimations in Dyudina et al. (2010, 2013) give the altitude of the lowest portion of the channel, which may extend vertically to higher altitudes. Here we assume that the charge centers are vertically separated by a few tens of kilometers, and up to a hundred kilometers. For this simple configuration we neglect wind shear effect, even though this factor may be important for cloud development and inhibit charge separation. We assume that the lightning channel is located between the base of the water ice cloud at 8 to 10 bars (130 to 160 km below the 1 bar level) and up to a 100 km above this altitude.

To estimate the relation between the lightning CMC and the dissipated energy we assume that the removed charge is concentrated within uniformly charged, non-overlapping identical spheres located one above the other, with a radius of a few tens of kilometers at most. The electrostatic energy stored by this configuration is given by:

$$U_p = \frac{2Q^2}{4\pi\epsilon_0}\left(\frac{3}{5R} - \frac{1}{2a}\right), \tag{3}$$

where Q is the total charge within each sphere, ϵ_0 is the permittivity of vacuum, R is the radius of the spheres and a is the vertical separation between the sphere centers ($a > 2R$).

ACCEPTED MANUSCRIPT

In analogy with the accepted definition of the CMC in the cloud-to-ground lightning on Earth, $M = Qa / 2$.

We tested this approach on terrestrial lightning, using simultaneous charge distribution and energy measurements of intra-cloud (IC) lightning discharges on Earth by Maggio et al. (2009). Equation (3) gives a good estimate of the energy released by IC discharges in the mature stage of the storm. Taking the energy constraint of lightning on Saturn into account, $M(t)$ can be ~ 10^4 to 10^5 C km when charge separation is of the order of a few 10-s km, and it can reach 10^6 C km in the extreme scenario where separation is 100 km.

3. The electron density profile on Saturn

The ambient electron density in the atmosphere determines the Maxwell relaxation time and the conditions for the onset of an electron avalanche. The electron density profile in planetary atmospheres is measured by means of radio occultation. Kliore et al. (2009) report the results of several radio occultations of Saturn, of which two are mid-latitude dawn profiles, and five are mid-latitude dusk profiles. According to Kliore et al. (2009) the dawn electron density (assumed to be equivalent to the night-time electron density according to Galand et al. 2009) at 1000 km is between 10^2 and 10^3 cm^{-3}, and dusk electron density is about an order of magnitude higher (all altitudes are with respect to the 1 bar pressure level, a common reference for the giant planets). Reliable measurements below 1000 km are not available (A. Nagy, personal communication).

Moore et al. (2004) modeled Saturn's ionosphere, predicting mid-latitude electron density at 18 hours local time (LT) of ~ 10^4 cm^{-3} at 1300 km, followed by a steep decrease at lower altitudes, and reaching 10^1 cm^{-3} at 1000 km. Moore et al. (2004) state that ion and electron densities do not change drastically during the night from that shown for 18 LT. An earlier model by Moses and Bass (2000) placed the base of the ionosphere

ACCEPTED MANUSCRIPT

at 600 km, assuming a photo-ionization of carbo-hydrates between 600 and 1000 km. Galand et al. (2009) extend the model described by Moore et al. (2004) to include the carbo-hydrate layer, predicting a fairly constant night-time (6 LT) electron density $N_e \sim 10^2$ cm^{-3} in the altitude range of 600 to 1000 km, followed by a steep decrease at lower altitudes. The low altitude electron density at 6 LT is one order of magnitude lower than at 18 LT in this model. None of these results can be compared with observations.

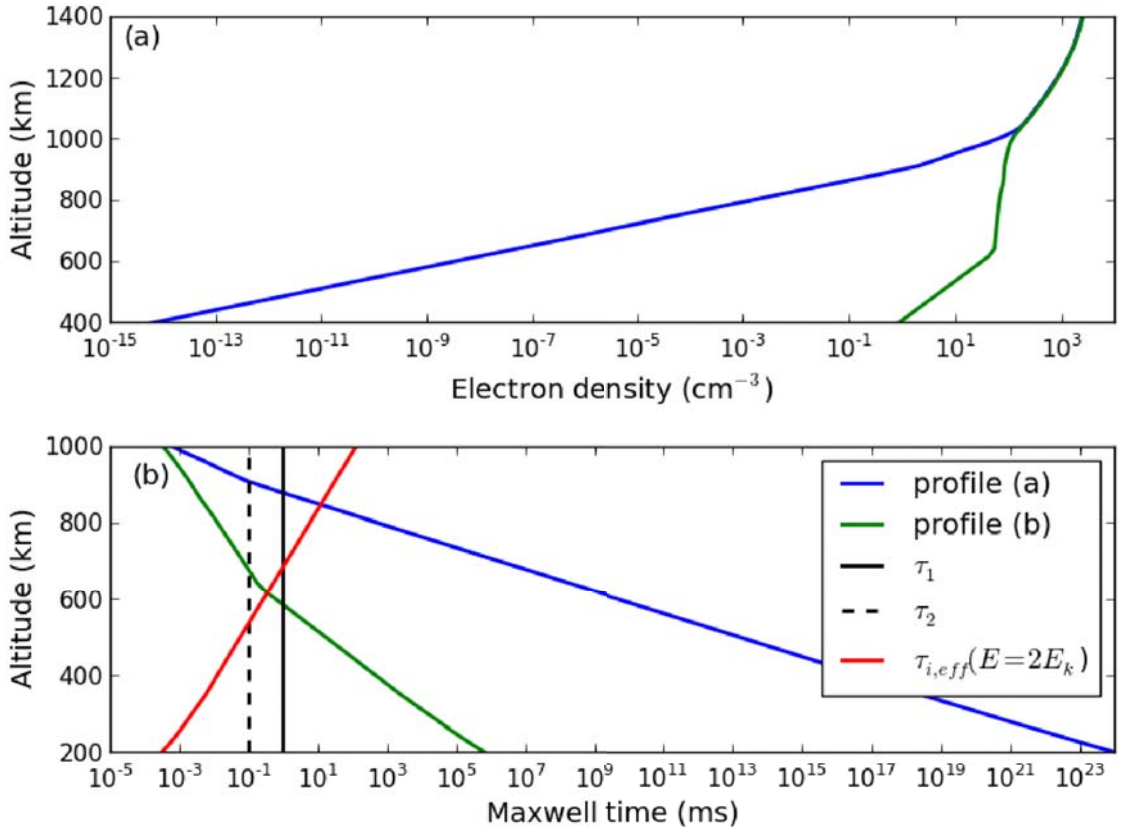

Figure 2: Panel (a): Night-time electron density for profiles (a) (blue) and profile (b) (green). Panel (b): Maxwell relaxation time according to profile (a) (blue) and profile (b) (green). The decay and rise times of the current are indicated (τ_1 and τ_2 from eq. (1) respectively). The effective ionization time as calculated for the electric field $E = 2E_k$ is plotted in red.

ACCEPTED MANUSCRIPT

ACCEPTED MANUSCRIPT

ACCEPTED MANUSCRIPT

For the purpose of modeling TLEs we need to know the night-time electron density profile in the lower ionosphere and the region below it, in the altitude range of 200 to 1000 km. We used two electron densities profiles, based on the models discussed above: profile (a) where we use the model results of Moore et al (2004) at 6 LT only down to 900 km, to model the absence of a CH4 layer; and profile (b), where the base of the ionosphere is at 600 km (Galand et al. (2009) 6 LT down to 600 km). The electron density is assumed to decrease exponentially below 900 km for profile (a) and below 600 km for profile (b) with scale heights of 30 and 55 km respectively. In Figure 2 we show the electron density (panel (a)), and the Maxwell relaxation time (panel (b)). Panel (b) is discussed in more detail in the next section.

4. Impact of electric fields on the lower ionosphere.

Electric breakdown in the upper atmosphere occurs if the reduced field E/N, where E is the field strength and N is the number density of neutral molecules, exceeds the conventional breakdown field at that altitude. The electric field induced by the lightning flash falls of as a power of the altitude z above the lightning flash, while the air density N decays exponentially, approximately as $\exp(-h/H)$, where H is the scale height of the atmosphere and h is the altitude above the reference level (here 1 bar); therefore the reduced electric field E/N increases with altitude. The conventional breakdown field E_k is defined by the competition between two opposing processes in the gas: impact ionization of neutrals by accelerated electrons, and attachment of electrons to certain molecules in the gas (O_2 on Earth, H_2 on Saturn). If the lightning induced electric field exceeds E_k below the ionosphere then ionization dominates, and electric breakdown can occur. This is the classical condition for the occurrence of sprites.

ACCEPTED MANUSCRIPT

This approach applies to the part of the atmosphere below a certain altitude that is essentially non-conducting, with a well conducting ionosphere further above. But in practice the atmospheric conductivity does not vanish completely at any altitude, forming a weakly conducting layer of several 10-s of kilometers on Earth, and probably several 100-s of kilometers on Saturn. In this region an electric field is electrically screened from a medium with conductivity σ within the Maxwell relaxation time, defined as $\tau_M = \epsilon_0/\sigma$, where ϵ_0 is the electric permittivity of vacuum. Maxwell screening time may be shorter than the time required for creating electron avalanches.

The electric conductivity σ is determined by the local electron density N_e and the neutral density N, $\sigma = e\,\mu_e\,N_e$. The electron mobility μ_e depends on the electric field and scales as $1/N$. As the local electron density increases, τ_M decreases respectively. The implications for terrestrial sprites were discussed in many papers, e.g. Pasko et al. (1998); Pasko and Stenbaek-Nielsen (2002); Qin et al. (2011); Sun et al. (2013). It is possible to distinguish between a weakly conducting region, where the lightning flash induces a descending ionization wave-front, which can be visible in the form of a halo; and an essentially non-conducting region where sprites can form (Pasko et al. (1998); Pasko and Stenbaek-Nielsen (2002)). Sun et al. (2013) introduce the ionization screening time as a generalization of the Maxwell time for ionizable media where the electron density and conductivity change during the electric screening process.

The attachment process in the hydrogen dominated atmosphere of Saturn, and other Gas Giants is inefficient (see e.g. Celiberto et al. (2001); Yoon et al. (2008)). This means that the conventional electric breakdown field is low, $E_k \sim 46$ Td (1 Td = 10^{-17} V cm^2). As a result, even if the electric field exceeds E_k, the effective ionization time may be longer than the local Maxwell relaxation time. This can be clearly seen in the example where $E=2E_k$ in Figure 2 (b).

ACCEPTED MANUSCRIPT

Therefore the comparison with the conventional breakdown field E_k is not the only relevant factor that determines the effect of the external field on the atmosphere. Rather, we must consider the three timescales involved in the process: the timescale τ_E, on which the external field rises, determined by the discharge process in the cloud; the Maxwell relaxation time τ_M, determined by the local conductivity; and the effective ionization time $\tau_i = 1 / \nu_{i,\mathrm{eff}} = 1/(\nu_i - \nu_a)$, where ν_i and ν_a are respectively the ionization and attachment rates. The ionization time depends on the local electric field and we define it only for $\nu_i > \nu_a$, i.e. for $E > E_k$. It is important to note that τ_M and τ_i depend dynamically on the local state of the atmosphere, including the electric field.

The first condition that must be satisfied for an appreciable impact of an applied electric field is that the electric field is not screened rapidly as it rises:

$$\tau_E \lesssim \tau_M, \tag{4}$$

with τ_M calculated from the initial conductivity. The electric field has two components which rise on different time scales: for the induction field $\tau_E = \tau_2$, the current rise time in eq. (1) and for the QES field $\tau_E = \tau_1$, the current decay time. If this condition does not hold, the electric field will be screened from the conducting region while it rises externally, so that it cannot penetrate into the conducting region. The induction field rises faster than the QES field, and therefore can penetrate to higher altitudes. But even if eq. (4) is satisfied, the field acts long enough to cause a significant increase of the electron density only if

$$\tau_M > \tau_i, \tag{5}$$

ACCEPTED MANUSCRIPT

a condition that we find useful to express in terms of a critical electric field E_c defined by the relation

$$\nu_{i,eff}(E_c/N) = \nu_i(E_c/N) - \nu_a(E_c/N) = \frac{e\mu_e N_e}{\epsilon_0} \quad (6)$$

so that eq. (5) reads $E > E_c$. We may check for this condition at any time but it is particularly relevant to investigate it when E is the bare (unscreened) external field and E_c reflects the initial electron density.

If the electric field is stationary after the fast initial rise, the Maxwell relaxation time can be generalized to the ionization screening time introduced by Sun et al. (2013) $\tau_{is} = \tau_i \log(1 + \tau_M / \tau_i)$. This definition takes the change of electron density and conductivity during the electric screening process into account; in general it is smaller than the Maxwell time τ_M and it reduces to τ_M if $\tau_M < \tau_i$, and $\Delta N_e = N_e(t) - N_e(0) \ll N_e(0)$.

Note that eq. (5) is a necessary condition for a significant *relative* increase in the electron density but it is not directly related to the *absolute* increase in ionization. In appendix (C) we show that the absolute increase in ionization caused by an electric field imposed instantaneously (i.e. $\tau_E \ll \tau_M$) and then kept constant is independent of the initial electron density and hence of E_c (see also Li et al. 2007). In this paper we are interested in conditions of low initial electron density where only a large relative increase in ionization causes the kind of impact that we are looking for, so eq. (5) still provides a useful criterion. Besides, a large relative increase in ionization represents a strong deviation from chemical equilibrium and, if it persists long enough, it may be detected by radio occultation techniques.

ACCEPTED MANUSCRIPT

The rates in eq. (6) and the electron mobility are found using the BOLSIG+ routine by Hagelaar and Pitchford (2005), using cross-sections from the Phelps compilation: H_2 - Buckman and Phelps (1985), Crompton et al. (1969); He - Crompton et al. (1967, 1970), Milloy and Crompton (1970), Hayashi (1981). The H_2 attachment cross–section was taken from Yoon et al. (2008). The rate coefficients, k_X, are plotted in Figure 3; they are independent of neutral density. The ionization and attachment rate coefficients are plotted on the left of Figure 3. The total effective ionization rate at a given altitude is $\nu_{i,\mathrm{eff}} = [H_2]k_{i,H2} + [He]k_{He} - [H2]k_{aH2}$, where k_X is the ionization coefficient in H_2, He, and the attachment coefficient in H_2; [X] is the density of the neutral species involved in the interaction. The conventional breakdown field E_k is found where $\nu_{i,\mathrm{eff}}$ equals 0; here it equals 46 Td. In the right panel of Figure 3 we plot the excitation rates to the states $H_2(a^3\Sigma_g^+)$ (UV-continuum) and H_2 ($d^3\Pi_u$) (the Fulcher band).

The neutral density in Saturn's mesosphere is deduced from an interpolation of two measured data sets (Festou and Atreya (1982)), and described by an exponential function $N = N_0 \exp(-h/H)$, where $N_0 = 3.5 \sim 10^{18}$ cm^{-3} and the scale height is $H = 65$ km.

In Figure 4 we show the reduced critical fields E_c/N for the two N_e profiles discussed in section 3, and the reduced conventional electric breakdown field E_k/N. The conventional breakdown field is proportional to the neutral density, and is represented by a vertical line at 46 Td. The left hand side of eq. (6) is negative if $E < E_k$, and therefore E_c is not defined at all altitudes. We identify the lowest altitude where E_c can be defined with the concept of a transition altitude as was proposed by Pasko *et al.* (1998). At this altitude the ionization, attachment and Maxwell times are of the same order of magnitude. Pasko and Stenbaek-Nielsen (2002) demonstrated how observed sprites can be used to estimate this altitude, and deduce the electron density there. Above the transition altitude streamers cannot develop, but halos can if the electric field is of the order of E_c or higher. Below the transition altitude streamers may develop if the induced electric field is larger than E_k.

ACCEPTED MANUSCRIPT

With profile (a) the transition altitude is approximately at 800 km, and with profile (b) it is at 500 km. If the external electric field exceeds E_k below the transition altitude, streamers have a chance to form there. Above the transition altitude the impact on the electron density and chemical composition would be appreciable if $E > E_c$.

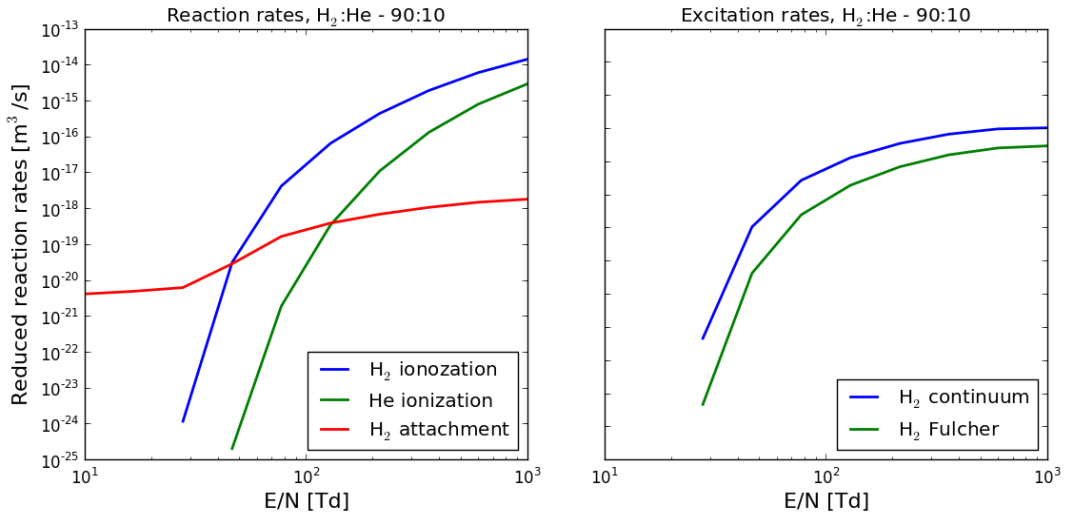

Figure 3: Rate coefficients as calculated by the BOLSIG+ routine for H_2:He – 90:10 (see references in text). The rate coefficient k_X of a two-body reaction X is related to the reaction rate ν_X by $\nu_X = k_X$ [X], where [X] the density of the neutral species involved. Left: Ionization in H_2 and He, and attachment in H_2. The conventional breakdown field E_k is determined where the attachment coefficient equals the ionization coefficient in H_2. Right: excitation rate coefficients of the states H_2 ($a^3\Sigma_g^+$) (UV-continuum) and H_2 ($d^3\Pi_u$) (the Fulcher band).

ACCEPTED MANUSCRIPT

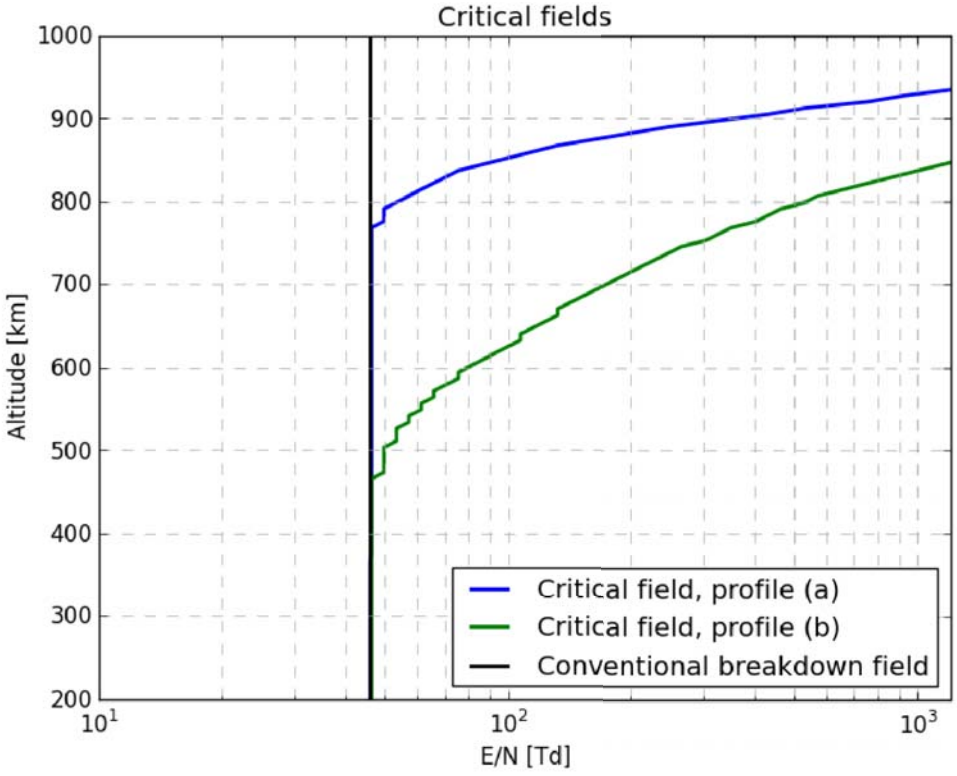

Figure 4: Reduced breakdown and critical fields (E_k and E_c). The breakdown field scales with neutral density N, therefore in reduced units it appears as a vertical line at 46 Td. The reduced critical field is calculated using equation (6).

5. Modeling electric fields in the upper atmosphere.

We model Saturn's atmospheric composition with 90% Hydrogen and 10% Helium. The homopause is located roughly at 1000 km above the 1 bar level, Nagy et al. (2009). The dominant interaction on the time scale of the lightning discharge and the simulation time (a few milliseconds) is the electron impact ionization, while the electron loss processes are slow, as discussed in the previous section (see Figure 3). We estimate the amount of photons emitted by a hypothetical TLE by calculating the density of excited hydrogen molecules: the transition H_2 ($d^3\Pi_u$) → H_2 ($a^3\Sigma_g^+$) emits the Fulcher bands, and

ACCEPTED MANUSCRIPT

H_2 ($a^3\Sigma_g^+$) → H_2 ($b^3\Sigma_u$) emits a continuum in the near UV. Non-radiative de-excitation processes such as collisional quenching with H_2 are negligible at the relevant altitudes (Thompson and Fowler (1972); Bretagne et al. (1981)). The excited molecules emit photons and relax to the ground state almost instantly; therefore the density of excited species can be used as the density of radiated photons (see Astashkevich and Lavrov (2002) for radiative life-times).

The electric field is computed by means of a self-consistent zero-dimensional model formulated in (Luque and Gordillo-Vázquez 2011, supplementary information). Under the assumptions of planar symmetry and the conservation of total current,

$$\partial_t E(t) = \partial_t E_p(t) - (\sigma/\epsilon_0)E(t), \tag{7}$$

where E is the total electric field, E_p is the field induced by the lightning flash, defined in section 2.2, equation (2). Electron drift is neglected. The conductivity $\sigma(t)$ depends on the local electron density N_e, which is determined by the rate equation

$$\partial_t N_e = \nu_i N_e. \tag{8}$$

Equations (7) and (8) are computed for each altitude separately.

The ambient electron densities at $t = 0$ (profiles (a) and (b)) are discussed in section 3. The duration of the parent lightning is important, as it determines the maximum intensity of the induced electric field, before it is screened by the local conductivity. In this work we use $\tau_2 = 0.1$ ms and $\tau_1 = 1$ ms, as discussed in section 2. We test three values for the total charge moment change: $M = 10^4$, 10^5 and 10^6 C km located at −110 km. Later in the text we refer to this model as the 1D model.

ACCEPTED MANUSCRIPT

The results are plotted in Figures 5 and 6 for profile (a) and profile (b) respectively. The plots are organized as follows: each row shows the output for a different CMC: (a) for $M = 10^4$ C km, (b) for $M = 10^5$ C km, and (c) for $M = 10^6$ C km (only in Figure 6, profile (b). The color plots on the left show the reduced electric field *E/N* as function of altitude (vertical axis) and the time elapsed after the start of the flash (horizontal axis). The electric field is retarded, as can be seen from the positive slope. The time step in these runs is 5 μs. The color scale is indicated to the right; scales are not identical. The plots on the right show the altitude profile of the electron density enhancement, $N_e(t) - N_e(0)$, five milliseconds after the beginning of the flash, and the cumulative densities of H_2 molecules emitting in the UV continuum and the Fulcher band at this time. Below we describe the results.

With profile (a) we used two CMC values, 10^4 and 10^5 C km (Figure 5). With $M = 10^4$ C km the electric field is higher than the critical field E_c (E_c is 100 Td at 850 km) above the transition altitude (at ~ 800 km). Photon and electron production at 900 km is less than 0.1 cm^{-3}, approximately 50% of initial electron density. Just below the transition altitude the electric field is a higher than E_k, reaching 60 Td at 780 km. With $M = 10^5$ C km considerable fields are obtained between 700 and 900 km, up to 1100 Td, stronger that the critical field E_c at the corresponding altitudes. The electron density is increased considerably; UV photon and electron production peak at 750 km with density ~ 30 and respectively 50 cm^{-3}. Below the transition altitude the electric field exceeds E_k. It is important to note here that the reaction rates are calculated in BOLSIG+ for electric fields smaller than 1200 Td. Above this field electrons approach relativistic energies, and the classical approach can no longer be applied. For this reason we do not test $M = 10^6$ C km with profile (a).

With Profile (b) we tried three CMC configurations, 10^4, 10^5 and 10^6 C km (Figure 6). With $M = 10^4$ C km the electric field is very low, there is no change in electron density, and no photon emission. With $M = 10^5$ C km the electric field does not exceed E_c above

ACCEPTED MANUSCRIPT

the transition altitude (~ 500 km) and the electron production is around 1% of the initial density. UV photon emission peaks at 700 km with 6 cm^{-3}. The electron density increases by less than 1 cm^{-3} at this altitude. Below the transition altitude E is lower than E_k, therefore streamers cannot form. In the extreme scenario $M = 10^6$ C km, the electric field reaches high values at a very short time, and decays fast, but a smaller time step leads to identical results. There is considerable electron and photon production in the entire range. Photon emissions peak at 500 km with 10^4 cm^{-3} and electron production at this altitude is near 3×10^3 cm^{-3}. Below the transition altitude electric field exceeds E_k.

The number of photons emitted by the event can be estimated, by multiplying the emission volume by the density of emitting species. The vertical and horizontal extents of all events are of the order of 100 km. Therefore with $M = 10^5$ C km and conductivity profile (a) the total number of photons is ~ (30 cm^{-3}) × (100 km)^2 × (100 km) ~ 3×10^{22} UV continuum photons. With profile (b) and $M = 10^5$ C km it is one order of magnitude less, ~ 6×10^{21} photons, and in the extreme scenario $M = 10^6$ C km, ~ 10^{25} photons can be emitted. The ISS camera on board Cassini is capable of detecting lightning with a total optical energy of 10^8 J (Dyudina et al. (2010)). These events where observed with the broad band filter, centered at 650 nm. Assuming all the photons have the same wavelength, this implies that an event which emits less than 10^{26} photons would not be detected.

When conventional breakdown field is exceeded below the transition altitude (Pasko et al. 1998), than streamers can form if the field persists for a long enough time. We find that with profile (a) this condition is met with both CMC values; with profile (b) the conventional breakdown field is exceeded below the transition altitude only for the extreme case of 10^6 C km. If streamers indeed form in these scenarios, a sprite can develop, which could be significantly brighter than the halo.

ACCEPTED MANUSCRIPT

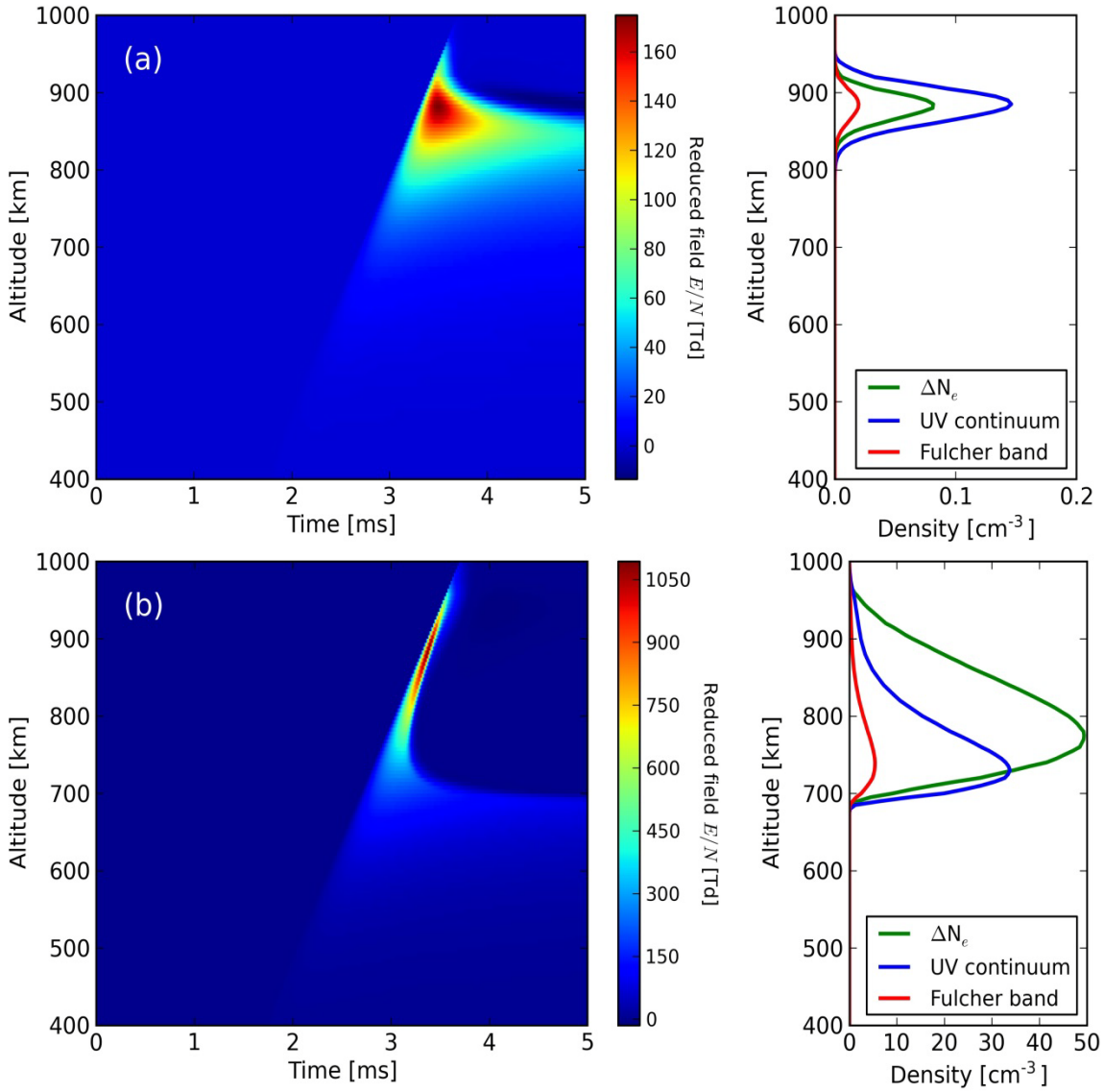

Figure 5: Output for profile (a): top row (a): $M = 10^4$ C km, bottom row (b): $M = 10^5$ C km. See details in text.

ACCEPTED MANUSCRIPT

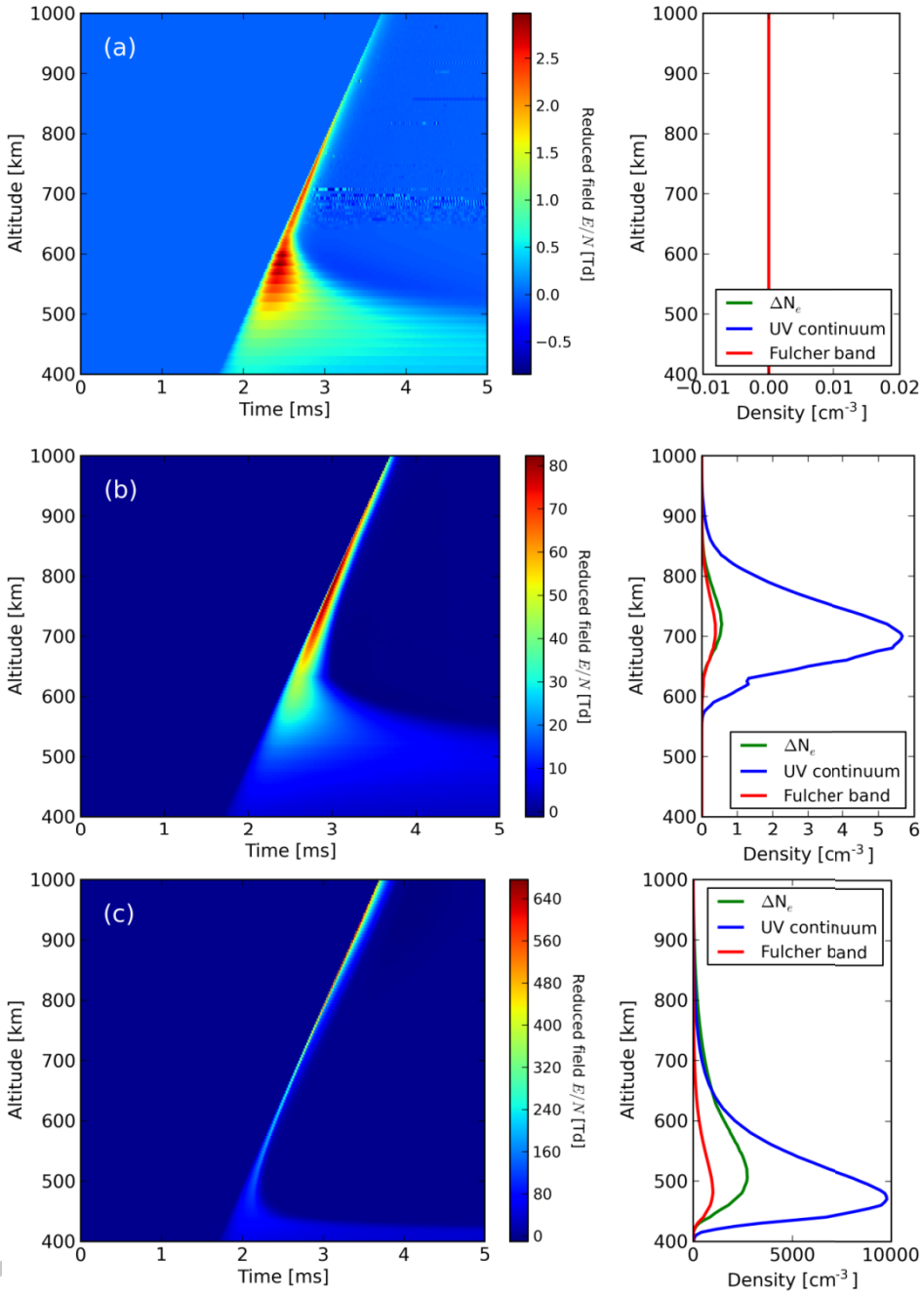

Figure 6: Output for profile (b): top row (a): $M = 10^4$ C km; middle row (b): M = 10^5 C km; bottom row (c): $M = 10^6$ C km. See details in text.

ACCEPTED MANUSCRIPT

6. The chemical impact of TLEs

The investigations about the possible existence of TLEs (sprites, halos and/or elves) in the upper atmosphere of Saturn requires the understanding of not only the plausible physical mechanisms underlying their generation but also should cover a rigorous analysis of the possible chemical influence of such upper atmospheric discharges in the mesosphere and lower ionosphere of Saturn. For doing that, we have developed a kinetic model in order to explore the chemical impact of transient H_2 (90%)/He (10%) plasmas generated by possible Saturnian TLEs.

The basic model equations controlling the non-equilibrium H_2/He plasma chemistry are a set of self-consistently solved time-dependent equations formed by the continuity equations for each of the species considered (ground neutrals, excited neutrals as well as positive and negative ions and electrons); the time-dependent, spatially-uniform Boltzmann equation controlling the energy distribution function of the free H_2/He plasma electrons; and equation (7) in section 5 to derive self-consistently the lightning-generated electric field. The present Saturnian TLE kinetic model is based on previous models that we have developed for the kinetics of TLEs on Earth (Gordillo-Vázquez (2008, 2010); Parra-Rojas et al. (2013)).

The Saturn kinetic model requires a set of electric and kinetic inputs. The electric inputs are the values (10^5 C km and 10^6 C km) considered for the charge moment changes (CMC) and the bi-exponential function shown in equation (1) in section 2 for the electric current flowing through the lightning channel, assuming a stroke duration (τ_1 = 1 ms) ten times longer than the current rise time (τ_2 = 0.1 ms). The kinetic inputs are basically the cross sections and rate coefficients needed for the different kinetic reactions considered in the calculations.

ACCEPTED MANUSCRIPT

The chemical species considered in this H_2/He global model for the plasma kinetics of possible Saturn TLEs are listed in appendix A. We have taken into consideration a total of 32 species classified into ground neutrals (3), electronically and vibrationally excited neutrals (21), electrons and negative ions (2) and positive ions (6). The exact number of reactions considered is 160, where there are electron-driven reactions (77), neutral-neutral reactions (41) including 11 Penning ionization mechanisms, ion-ion recombination mechanisms (9), ion-neutral processes (18, with 16 positive ion-neutral reactions and 2 negative ion-neutral reactions) and radiative spontaneous de-excitation channels (15). The complete list of all the reactions considered and their corresponding rate coefficients are shown in appendix B. There are 48 electron-impact reactions indicated as electron energy distribution function (EEDF)-dependent processes for which their rate coefficients are not shown explicitly because they are self-consistently calculated using available cross sections. The reference of each of the cross-sections and/or rates used for all the considered reactions is indicated in the last column of each of the tables in appendix B. At the present stage the model does not include photochemistry (night-time conditions are assumed) nor diffusion.

In modeling the kinetics of hydrogen plasmas we have also considered electron impact dissociative attachment of H_2. Although the cross section for dissociative attachment of H_2 is quite small for the lowest vibrational level of the ground electronic state ($H_2(X^1\Sigma^+_g, v = 0)$), they increase rapidly with increasing vibrational levels (Bardsley and Wadehra (1979)). Since the attachment cross sections show a peak ($\sigma_{peak}(v)$) at the threshold energies ($\varepsilon_{th}(v)$) and a fast reduction in magnitude as the energy is increased above the threshold, Celiberto et al. (2001) proposed to fit the attachment cross section of $H_2(X^1\Sigma^+_g, v)$ just above the threshold by the convenient analytic expression $\sigma_{DA}(\varepsilon) = \sigma_{peak}(v) \exp(-(\varepsilon - \varepsilon_{th}(v))/\varepsilon_g)$ with $\varepsilon_g = 0.45$ eV. We considered dissociative attachment

ACCEPTED MANUSCRIPT

cross sections of H_2 ($X^1\Sigma^+_g$, v) up to $v = 9$ using the values of $\sigma_{peak}(v)$ and $\varepsilon_{th}(v)$ given by Bardsley and Wadehra (1979).

The kinetic model covers the altitude range between 450 km and 1000 km above Saturn's 1 bar level. We considered electron and neutral density as discussed above, and used the same settings (except $M = 10^4$ C km) as in Figures 5 and 6. The gas temperature (T_g) is considered to be constant and equal to 125 K (Nagy et al. (2009) for the altitudes investigated with this model, and we assumed that possible TLEs in Saturn occur below the thermosphere. Finally, the plasma is assumed to be optically thin ($\kappa = 1$) and the plasma kinetics is simulated during 5 ms.

The results for the electron density and the different ion concentrations obtained from the kinetic model are shown in Figure 7 for the altitudes in which, for each of the cases considered, the electron density reaches its highest value. In plotting Figure 7, we have considered the $M = 10^5$ C km and 10^6 C km cases shown in Figures 5 and 6. Panels (b) and (d) of Figure 7 show the ion concentrations for $M = 10^5$ C km at 750 km and 700 km with, respectively, electron density profiles (a) and (b), and in the lower panel (f) we have used $M = 10^6$ C km at 500 km with the electron density profile (b). The initial concentrations of all ions are zero except for H_2^+ which, at $t = 0$ sec, is assumed the same as the initial electron density considered. Note that panels (a), (c) and (e) of Figure 7 represent the reduced electric field (E/N) versus time for, respectively, the altitudes 750 km, 700 km and 500 km, with corresponding ion kinetics shown in panels (b), (d) and (f).

The first feature we notice in the three cases shown in Figure 7 is that the electron density enhancement ($N_e(t) - N_e(0)$) at t = 5 ms is the same as the one obtained with the 1D dynamic model described in section 5. Moreover, it is interesting to note that while the dominant source of electrons is electron impact ionization of H_2 producing H_2^+, we

ACCEPTED MANUSCRIPT

note that H_2^+ ions are quickly (between one and several tens of microseconds) converted to H_3^+ ions through the fast reaction $H_2^+ + H_2 \rightarrow H_3^+ + H$ so that H_3^+ becomes the dominant ion. It can be seen in Figure 7 that the higher the altitude, the longer the time the lightning originated electromagnetic pulse takes to travel from the thundercloud layer (see panels (a), (c) and (e)). Consequently, the kinetic influence triggered by the arriving electric field initiates with a slight delay at 750 km (upper panel) than at 500 km (lower panel). When CMC remains the same (10^5 C km) and profiles (a) and (b) are compared (shown in panels (b) and (d) of Figure 7) the concentration of the positive ion He^+ after t = 3 ms is the highest one after that of H_3^+ with profile (a) while it is negligible with profile (b). However, when profile (b) is used as the initial electron density profile and the CMC increases from 10^5 C km at 700 km to 10^6 C km at 500 km (panels (d) and (f) in Figure 7) the reduced electric field (E/N) increases from about 65 Td to 125 Td (see panels (c) and (e) of Figure 7). The latter significant increase of the field when $M = 10^6$ C km produces a sharp growth of more than two orders of magnitude in the ambient electron density up to nearly 3500 cm^{-3} (see lower panel in Figure 7). During the field duration, direct electron impact ionization drives the production of electrons. However, once the field is off after 3.20 ms (upper panel in Figure 7), 3.00 ms (panel (c) in Figure 7) and 2.25 ms (panel (e) in Figure 7), the production of electrons is dominated by Penning ionization, $He(2s^2\ ^3S) + H_2 \rightarrow H_2^+ + He + e$ and $He(2s^2\ ^3S) + H_2 \rightarrow H + HeH^+ + e$, when $M = 10^5$ C km with profile (a) is used, and by electron detachment, $H^- + He \rightarrow H + He + e$, when $M = 10^5$ C km and $M = 10^6$ C km with profile (b) are used.

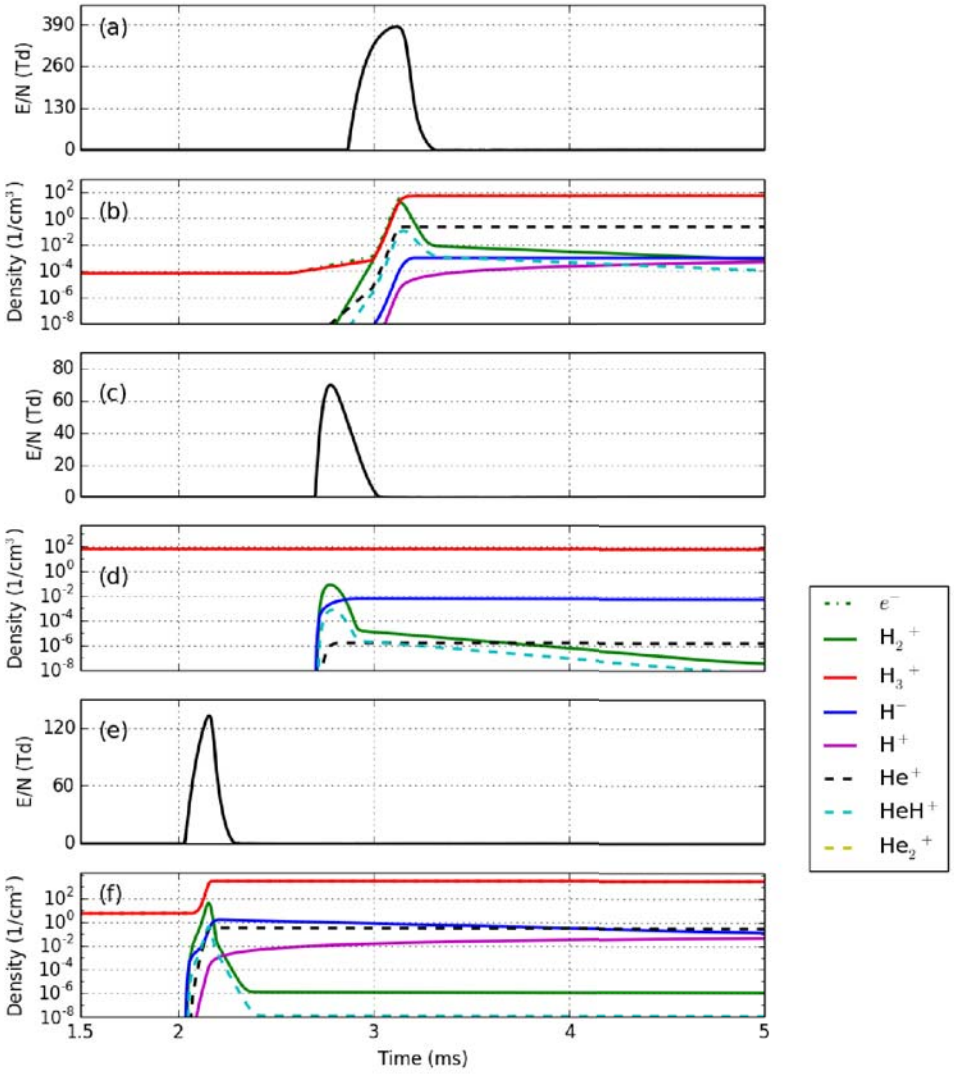

Figure 7: Reduced electric field (E/N), electron and ion concentrations as a function of time calculated with the kinetic model for $M = 10^5$ C km (profiles (a) and (b)) and $M = 10^6$ C km (profile (b)). The plots are calculated for the altitudes where the induced electron density reaches its highest values, that is, 750 km (panels (a) and (b)), 700 km (panels (c) and (d)) and

ACCEPTED MANUSCRIPT

500 km (panels (e) and (f)). Note that the lines for the concentration of H_3^+ ions and electrons coincide. The dashed line (electrons) is hidden by the line of H_3^+. Concentrations below 10^{-8} cm^{-3} are not plotted.

The increase of the concentration of H^+ right after the end of the electric field pulse in panels (b) and (f) is due to $He^+ + H_2 \rightarrow H^+ + H + He$. However, the behavior of H^- after the end of the electric field pulse changes when different CMCs and initial electron density profiles are used. In this regard, H^- remains constant or decreases when $M = 10^5$ C km and profile (a), or $M = 10^6$ C km and profile (b) are used. This is connected to the electron detachment loss rate of the H^- previously produced by electron attachment ($e + H_2 \rightarrow H^- + H$) when the field is on: a small or a high loss rate with respect to the H^- field-dependent attachment production rate keeps H^- constant (see panels (b) and (d)) or makes H^- decrease (lower panel), respectively.

The concentrations of the helium ions considered (He^+, He_2^+ and HeH^+) are usually very small except for He^+ when $M = 10^5$ C km and profile (a) (panel (b) of Figure 7) and $M = 10^6$ C km and profile (b) (lower panel of Figure 7) are used; in those cases, He^+ becomes the second most important positive ion after H_3^+ for $t > 3$ ms and 4 ms, respectively.

We show in Figures 8 and 9, the altitude-dependent instantaneous and cumulative number of H_2 continuum (UV) and Fulcher photons calculated with the full kinetic model presented in this paper. The panels in the left and right hand sides of Figures 8 and 9 correspond respectively to the UV and Fulcher emissions associated to the same CMC and ambient electron density profiles discussed in Figure 7. In general, both UV and Fulcher emissions are very fast with UV emissions being slightly stronger than the Fulcher ones. In Figure 8, where the instantaneous emissions are represented, it is interesting to note that both types of optical emissions are a bit longer for lower altitudes. The latter effect (longer optical emissions at lower altitudes) is related to the slower

ACCEPTED MANUSCRIPT

relaxation times at these altitudes. On the other hand, the cumulative number of UV photons calculated with the kinetic model (see Figure 9) gives the same values as those obtained with the 1D dynamic model, except for the number of UV photons calculated with $M = 10^5$ C km using profile (b) where a difference of less than factor two is found. If the base of the ionosphere is at 1000 km (profile (a)) above the 1 bar level, the kinetic model predicts 40 and 6 UV and Fulcher photons cm^{-3}, respectively, at 700 km with $M = 10^5$ C km. However, if the base of the ionosphere is at 600 km (profile (b)), the kinetic model predicts ~ 9 and ~ 0.6 UV and Fulcher photons cm^{-3}, respectively, at 680 km with $M = 10^5$ C km, and ~ 10,000 and ~ 1000 UV and Fulcher photons cm^{-3}, respectively, at 475 km with $M = 10^6$ C km.

We have also calculated (not shown) the concentration of H (n=3) and the corresponding cumulative number of Balmer photons cm^{-3} (656.28 nm), which is two orders of magnitude lower than the number of continuum H_2 UV photons.

ACCEPTED MANUSCRIPT

ACCEPTED MANUSCRIPT

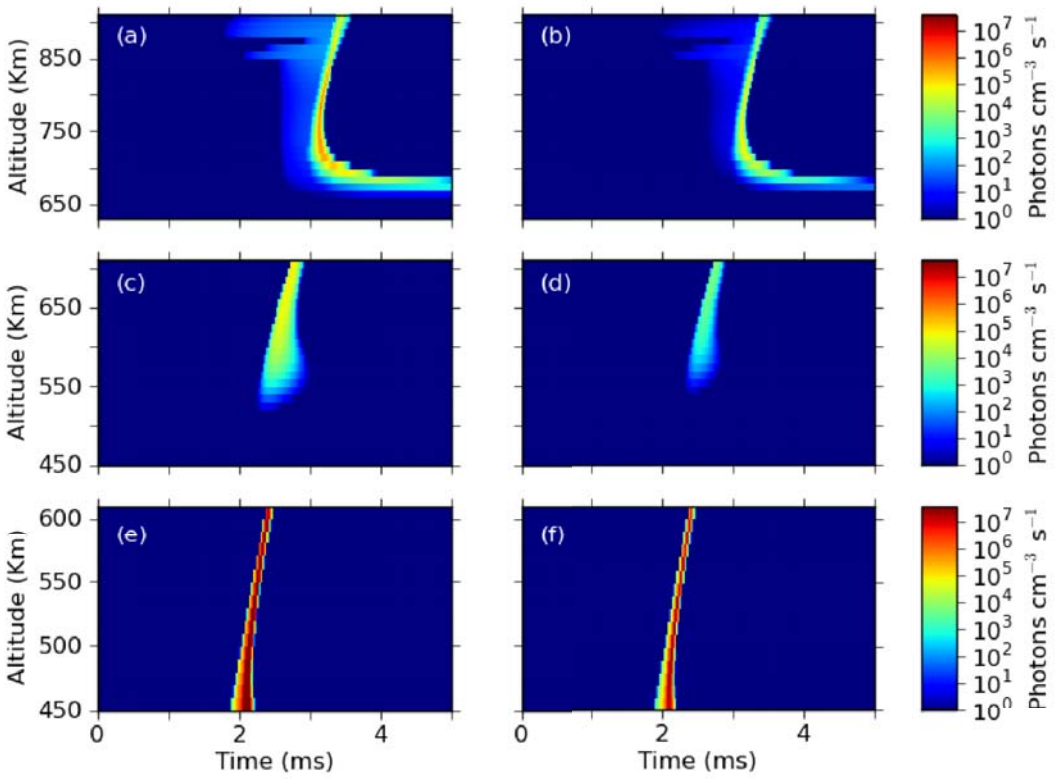

Figure 8: Altitude dependent instantaneous number of UV continuum (left hand side panels) and Fulcher band (right hand side panels) photons cm^{-3} s^{-1}, calculated with the kinetic model for the same CMC and ambient electron density profiles as in Figure 7.

ACCEPTED

ACCEPTED MANUSCRIPT

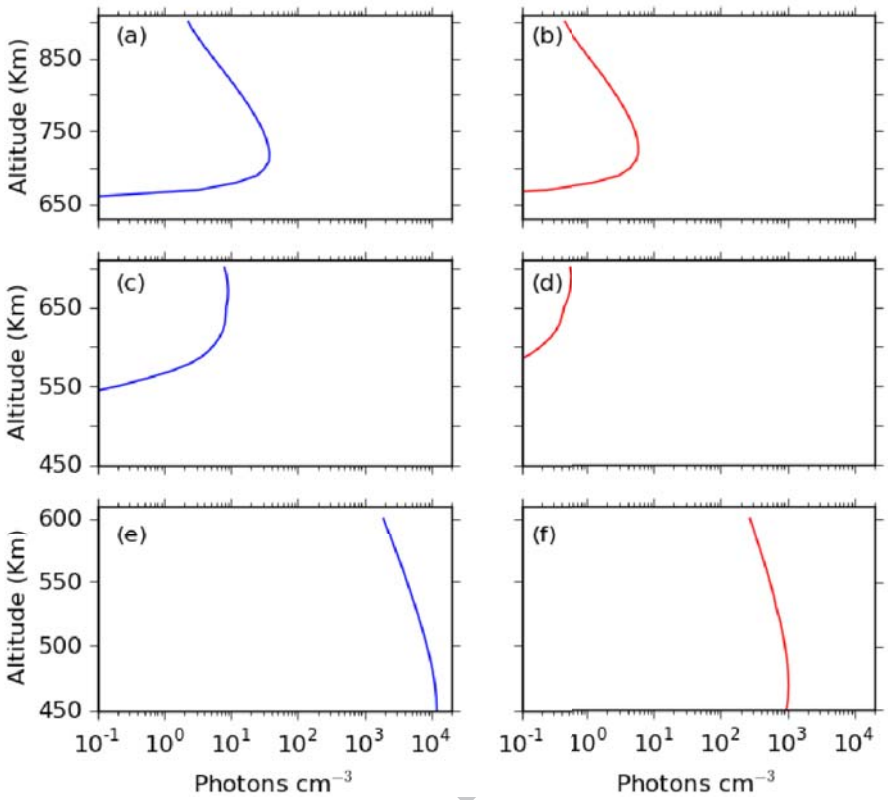

Figure 9: Altitude dependent cumulative number of UV continuum (left hand side panels) and Fulcher band (right hand side panels) photons per cm^3, calculated with the kinetic model for the same CMC and ambient electron density profiles as in Figure 7.

ACCEPTED

ACCEPTED MANUSCRIPT

7. Discussion and conclusions

In this work we examine the impact of lightning in Saturn's atmosphere on the planet's lower ionosphere. We review the known constraints on the energies and locations of lightning flashes and the conductivity and electron density profiles of Saturn's atmosphere in sections 2 and 3. Within these constraints, we suggest that charge moment change of these lightning flashes can range from 10^4 to 10^5 C km, with 10^6 C km as an extreme scenario. We assume that the lightning flash depth is at -110 km below the 1 bar pressure level, a region where deep convective H_2O clouds reside. According to models, it appears that the electron density is strongly decreased below 1000 km above the 1 bar level, however this effect is yet to be measured. We use existing models to simulate two possible electron density profiles; one places the bottom of the ionosphere around 1000 km, and the other at 600 km above the 1 bar level.

In the conventional breakdown approach, electrical breakdown in the gas occurs when the induced electric field exceeds E_k. In section 4 we show that in Saturn's mesosphere an electric field higher than E_k may not cause a significant increase of the local electron density, if the electric field screening is faster than ionization. We express this condition in terms of a critical electric field E_c, based on the competition between two time scales – the initial Maxwell relaxation time and the typical ionization time. If the induced electric field exceeds E_c, then the electron density can grow by several orders of magnitude, but if it is smaller than E_c then the relative growth of the local electron density is small. Photons are produced also when $E < E_c$; if the initial electron density is high, then a considerable amount of photons could be emitted. This is an additional constraint on the formation of halos in the weakly conducting atmosphere, above the transition altitude (as defined by Pasko et al. (1998)). At transition altitude the Maxwell relaxation time is comparable with ionization and attachment times at $E = E_k$, and $E_c \sim$

ACCEPTED MANUSCRIPT

E_k, below this altitude E_c is not defined; in other words the conductivity of the atmosphere can be neglected. Above the transition altitude Maxwell screening of the electric field limits the ionization reactions as well as the magnitude of the applied field. Below the transition altitude sprites may form if the electric field exceeds E_k.

The modeling of halos and sprites on Earth is generally based on the quasi-electrostatic heating model of the lower ionosphere (Pasko et al. (2012)). It is generally assumed that the electric field is determined by the charge moment change of the flash, and sets in immediately at all altitudes. This assumption works well for the short distances on Earth, where $z < 100$ km. The electric field reaches its maximum on the time scale of the flash duration (τ_2 in equation (1), see Figure 1). At higher altitudes, where neutral density is lower, the reduced electric field exceeds breakdown conditions (E_k and E_c) earlier than at lower altitudes. The result is the formation of the well documented downward propagating halo.

On planets with larger atmospheric scale heights, such as Saturn, where the relevant length scales are on the order of several hundreds of kilometers, the propagation of the field in space cannot be neglected (in other words, it cannot be assumed to be immediate). Moreover, at a distance longer than 100 km the radiation and induction components of the retarded field are significantly stronger than the quasi electro-static (QES) component (see section 2.2). Directly above the vertical lightning channel the dominant component is the induction field. In our analysis we find that a halo in Saturn's atmosphere would propagate upward.

In section 5 we use a self-consistent one-dimensional model to calculate the effect of the electric field on the electron density, the photon production, and the altitude range of the event. We test several case studies based on the limited knowledge of Saturn's electron conductivity profile at the bottom side of the ionosphere, and the lightning flash characteristics. With profile (a), where the base of the ionosphere is around 1000 km, we

ACCEPTED MANUSCRIPT

find that a very faint halo may be produced by $M = 10^4$ C km; with $M = 10^5$ C km electron density grows by orders of magnitude, but since the initial electron density is very low the density of produced photons is ~ 30 cm^{-3} in the altitude range of 700 to 800 km above the 1 bar level. In both scenarios E exceeds E_k below the transition altitude (800 km), suggesting that streamers may form there. However, this needs to be tested further with a more detailed model.

With profile (b) where the base of the ionosphere is around 600 km, we find that a charge moment change $M = 10^4$ C km is screened completely by the ionosphere. With $M = 10^5$ C km the electric field exceeds E_k above ~ 600 km but does not exceed E_c. As a result the electron density increases by about 1%. The initial electron density above 600 km is ~ 10^1 cm^{-3}, as a result a faint halo is created with a peak photon production at 700 km, 5 cm^{-3}. With this profile we test also the extreme scenario of $M = 10^6$ C km. In this scenario the electric field increases considerably in the entire range; peak photon production is at 500 km, with 10^4 cm^{-3} UV photons. With profile (b) E_k is exceeded below the transition altitude (500 km) only in the extreme case $M = 10^6$ C km.

We conclude that faint halos may form in both cases, and therefore for any intermediate electron density profile. The brightest halos would be created by $M = 10^5$ C km with profile (a), with a total number of emitted photons of the order of 10^{22}, and by $M = 10^6$ C km with profile (b), with ~ 10^{25} photons. Either of these events is below the current observation limit of the ISS camera on-board the Cassini spacecraft. On the other hand, sprites may form if the ionosphere is closer in nature to profile (a). On Earth sprites typically emit considerably more light than halos due to the local enhancement of the electric field (see e.g. Kuo et al. (2008), Luque and Ebert (2009)). If a sprite-like TLE is observed on Saturn, it would suggest that the carbo-hydrate photo-ionization layer is weaker than suggested in Galand et al. (2009). Based on geometric considerations we would expect the halo to extend at least a 100 km in radius in the lateral direction; a sprite would be much more concentrated.

ACCEPTED MANUSCRIPT

In section 6 we present a self-consistent kinetic model that was developed to analyze the atmospheric chemical disturbances caused by possible Saturnian upper atmospheric electric discharges. We have used our kinetic model in the same conditions used in the 1D dynamic model and calculated the altitude and time-dependent behavior of the electron and ion densities together with the instantaneous and cumulative number of photons emitted by H_2 UV continuum and Fulcher bands originated by a halo-like event in Saturn's mesosphere. We found that H_3^+ ions are rapidly produced from the parent H_2^+ ions through the fast reaction $H_2^+ + H_2 \rightarrow H_3^+ + H$, so that H_3^+ becomes the dominant ion in all the scenarios considered. We also found that after 4 ms, the concentration of the positive ion He^+ becomes the second largest (after H_3^+) when we use $M = 10^5$ C km with profiles (a) and $M = 10^6$ C km with profile (b). The maximum total number of UV and Fulcher photons from a possible Saturnian halo predicted with our full kinetic model are, respectively, 10^{25} and 10^{24} when $M = 10^6$ C km and profile (b) are used.

Our analysis in section 2 shows that $M = 10^6$ C km can fit the observed discharge energy (~ 10^{12} – 10^{13} J), but only if the lightning channel is long, of the order of a hundred kilometers, otherwise the uniform charge cells would overlap. Whether such a large separation is possible remains to be determined; either by detailed modelling which includes cloud microphysics, or by new observations. It seems that detectable halos are unlikely in Saturn's atmosphere, but there is a possibility of sprites if the conventional breakdown field is exceeded below the transition altitude. The altitude of the event above the cloud tops could be estimated if images are taken towards the planet's limb. The lower boundary of a halo can be used to estimate the transition altitude. Such observations could be used to probe the local electron density.

Acknowledgments

We would like to thank G. Fischer for his helpful input on Saturnian lightning. We wish to thank the anonymous reviewers for their in-depth comments.

ACCEPTED MANUSCRIPT

The work of DD and YY is supported by the Israeli Ministry of Science scholarship in Memory of Col. Ilan Ramon, the Research Authority of the Open University of Israel, and by the Israeli Science Foundation grant 117/09. Cooperation was facilitated by the support of the European Science Foundation, grant no 5269. The work by AL, FJGV and FCPR is supported by the Spanish Ministry of Science and Innovation, MINECO under project AYA2011-29936-C05-02 and by the Junta de Andalucia under Proyecto de Excelencia FQM-5965. AL is supported by a Ramón y Cajal contract, code RYC-2011-07801 and FCPR acknowledges MINECO for a FPI grant, code BES-2010-042367.

Bibliography

Astashkevich, S., Lavrov, B., 2002. Lifetimes of the electronic-vibrational-rotational states of hydrogen molecule (review). Optics and Spectroscopy 92 (6), 818.

Atreya, S. K., 1986. Atmospheres and ionospheres of the outer planets and their satellites. Vol. 15. Springer Verlag, Springer Series on Physics Chemistry Space.

Atreya, S. K., Wong, A.-S., 2005. Coupled clouds and chemistry of the giant planets - a case for multiprobes. Space Science Reviews 116 (1-2), 121.

Bardsley, J., Wadehra, J., 1979. Dissociative attachment and vibrational excitation in low-energy collisions of electrons with H_2 and D_2. Physical Review A 20 (4), 1398.

Bretagne, J., Godart, J., Puech, V., 1981. Time-resolved study of the H_2 continuum at low pressures. Journal of Physics B: Atomic Molecular Physics 14, L761.

Bruce, C., Golde, R., 1941. The lightning discharge. Electrical Engineers - Part II: Power Engineering, Journal of the Institution of, IET, 88, 487.

ACCEPTED MANUSCRIPT

Buckman, S.J. and Phelps, A.V., 1985. JILA Information Center Report No. 27, University of Colorado; J. Chem. Phys. 82, 4999.

Celiberto, R., Janev, R. K., Laricchiuta, A., Capitelli, M., Wadehra, J. M., Atems, D. E., 2001. Cross section data for electron-impact inelastic processes of vibrationally excited molecules of hydrogen and its isotopes. Atomic Data and Nuclear Data Tables 77 (2), 161.

Crompton, R. W., Elford, M. T., Jory, R. L., 1967. The momentum transfer cross section for electrons in helium, Australian Journal of Physics. 20, 369. Phelps database, www.lxcat.net, retrieved on October 23, 2013.

Crompton, R. W., Gibson, D. K., McIntosh, A. I., 1969. The Cross Section for the J = 0→2 Rotational Excitation of Hydrogen by Slow Electrons, Australian Journal of Physics, 22, 715. Phelps database, www.lxcat.net, retrieved on October 23, 2013.

Crompton, R. W., Elford, M. T., Robertson, A. G., 1970. The momentum transfer cross section for electrons in helium derived from drift velocities at 77° K; Australian Journal of Physics, 23, 667.

Cummer, S. A., Jaugey, N., Li, J., Lyons, W. A., Nelson, T. E., Gerken, E. A., 2006. Submillisecond imaging of sprite development and structure. Geophys. Res. Lett. 33, 4104.

Dyudina, U., Ingersoll, A., Ewald, S., Porco, C., Fischer, G., Kurth, W., West, R., 2010. Detection of visible lightning on Saturn. Geophys. Res. Lett. 37, L09205.

Dyudina, U. A., Ingersoll, A. P., Ewald, S. P., Porco, C. C., Fischer, G., Yair, Y., 2013. Saturn's visible lightning, its radio emissions, and the structure of the 2009 - 2011 lightning storms. Icarus 226 (1), 1020.

ACCEPTED MANUSCRIPT

Farrell, W., Kaiser, M., Fischer, G., Zarka, P., Kurth, W., Gurnett, D., 2007. Are Saturn electrostatic discharges really superbolts? a temporal dilemma. Geophys. Res. Lett. 34 (6), L06202.

Festou, M. C., Atreya, S. K., 1982. Voyager ultraviolet stellar occultation measurements of the composition and thermal profiles of the Saturnian upper atmosphere. Geophys. Res. Lett. 9, 1147.

Fischer, G., Desch, M., Zarka, P., Kaiser, M., Gurnett, D., Kurth, W., Macher, W., Rucker, H., Lecacheux, A., Farrell, W., et al., 2006. Saturn lightning recorded by Cassini/RPWS in 2004. Icarus 183 (1), 135.

Fischer, G., Gurnett, D., Kurth, W., Akalin, F., Zarka, P., Dyudina, U., Farrell, W., Kaiser, M., 2008. Atmospheric electricity at Saturn. Space Science Reviews 137 (1), 271.

Fischer, G., Kurth, W., Dyudina, U., Kaiser, M., Zarka, P., Lecacheux, A., Ingersoll, A., Gurnett, D., 2007. Analysis of a giant lightning storm on Saturn. Icarus 190 (2), 528.

Fischer, G., Kurth, W., Gurnett, D., Zarka, P., Dyudina, U., Ingersoll, A., Ewald, S., Porco, C., Wesley, A., Go, C., et al., 2011. A giant thunderstorm on Saturn. Nature 475 (7354), 75.

Galand, M., Moore, L., Charnay, B., Mueller-Wodarg, I., Mendillo, M., 2009. Solar primary and secondary ionization at Saturn. J. Geophys. Res. 114 (A6), A06313.

Gordillo-Vázquez, F. J., 2008. Air plasma kinetics under the influence of sprites. Journal of Physics D: Applied Physics 41 (23), 234016.

ACCEPTED MANUSCRIPT

ACCEPTED MANUSCRIPT

Gordillo-Vázquez, F. J., 2010. Vibrational kinetics of air plasmas induced by sprites. J. Geophys. Res. (Space Physics), 115 (A5), A00E25.

Hagelaar, G., Pitchford, L., 2005. Solving the Boltzmann equation to obtain electron transport coefficients and rate coefficients for fluid models. Plasma Sources Science and Technology 14 (4), 722.

Hayashi, M., 1981. Report No. IPPJ-AM-19 1981, Institute of Plasma Physics, Nagoya University. Phelps database, www.lxcat.net, retrieved on October 23, 2013.

Itikawa database, www.lxcat.net, retrieved on October 23, 2013.

Kliore, A., Nagy, A., Marouf, E., Anabtawi, A., Barbinis, E., Fleischman, D., Kahan, D., 2009. Midlatitude and high-latitude electron density profiles in the ionosphere of Saturn obtained by Cassini radio occultation observations. J. Geophys. Res. 114 (A4), A04315.

Li, C., Brok, W. J. M., Ebert, U., and van der Mullen, J. J. A. M, 2007. Deviations from the local field approximation in negative streamer heads. J. Geophys. Res. 101, 123305.

Luque, A., Ebert, U., 2009. Emergence of sprite streamers from screening-ionization waves in the lower ionosphere. Nature Geosciences 2, 757.

Luque, A., Gordillo-Vázquez, F. J., 2011. Mesospheric electric breakdown and delayed sprite ignition caused by electron detachment. Nature Geoscience 5, 22.

Maggio, C., Marshall, T., Stolzenburg, M., 2009. Estimations of charge transferred and energy released by lightning flashes. J. Geophys. Res. 114, D14203.

ACCEPTED MANUSCRIPT

Milloy, H. B., Crompton, R. W., 1977. Momentum-transfer cross section for electron-helium collisions in the range 4-12 eV; Physical Review A, 15, 1847. Phelps database, www.lxcat.net, retrieved on October 23, 2013.

Moore, L., Mendillo, M., Müller-Wodarg, I., Murr, D., 2004. Modeling of global variations and ring shadowing in Saturn's ionosphere. Icarus 172 (2), 503.

Moses, J., Bass, S., 2000. The effects of external material on the chemistry and structure of Saturn's ionosphere. J. Geophys. Res. 105 (E3), 7013.

Nagy, A. F., Kliore, A. J., Mendillo, M., Miller, S., Moore, L., Moses, J. I., Müller-Wodarg, I., Shemansky, D., 2009. Upper atmosphere and ionosphere of Saturn. In: Saturn from Cassini-Huygens. Springer, pp. 181.

Parra-Rojas, F. C., Luque, A., Gordillo-Vázquez, F. J., 2013. Chemical and electrical impact of lightning on the earth mesosphere: The case of sprite halos. J. Geophys. Res. (Space Physics), 118, 1.

Pasko, V. P., Inan, U. S., Bell, T. F., 1998. Spatial structure of sprites. Geophys. Res. Lett. 25 (12), 2123.

Pasko, V. P., Stenbaek-Nielsen, H. C., 2002. Diffuse and streamer regions of sprites. Geophys. Res. Lett. 29 (10), 1440.

Pasko, V. P., Yair, Y., Kuo, C.-L., 2012. Lightning related transient luminous events at high altitude in the earth's atmosphere: phenomenology, mechanisms and effects. Space Science Review 168 (1-4), 475.

ACCEPTED MANUSCRIPT

ACCEPTED MANUSCRIPT

Qin, J., Celestin, S., Pasko, V. P., 2011. On the inception of streamers from sprite halo events produced by lightning discharges with positive and negative polarity. J. Geophys. Res. (Space Physics), 116 (A6), 1978.

Sánchez-Lavega, A., del Río-Gaztelurrutia, T., Hueso, R., Gómez-Forrellad, J., Sanz-Requena, J., Legarreta, J., García-Melendo, E., Colas, F., Lecacheux, J., Fletcher, L., et al., 2011. Deep winds beneath Saturn's upper clouds from a seasonal long-lived planetary-scale storm. Nature 475 (7354), 71.

Sayanagi, K. M., Dyudina, U. A., Ewald, S. P., Fischer, G., Ingersoll, A. P., Kurth, W. S., Muro, G. D., Porco, C. C. and West, R. A., 2013. Dynamics of Saturn's great storm of 2010-2011 from Cassini ISS and RPWS. Icarus 223 (460-478), *doi:* 10.1016/j.icarus.2012.12.013.

Sentman, D. D., 2004. Electrical breakdown parameters for neutral atmospheres of the solar system. ISUAL workshop proceedings, 08-O13-O016.

Sun, A. B., J. Teunissen, and U. Ebert (2013), Why isolated streamer discharges hardly exist above the breakdown field in atmospheric air, Geophys. Res. Lett., 40, 2417, *doi:*10.1002/grl.50457.

Thompson, R. T., Fowler, R. G., 1972. Lifetime and quenching rates for the H_2 continuum. J. Quant. Spectrosc. Radiat. Transfer. 12, 117.

Uman, M. A., 2001. The lightning discharge. Courier Dover Publications.

Wilson, C. T. R., 1925. The electric field of a thundercloud and some of its effects. Proc. Phys. Soc. London 37, 32D.

ACCEPTED MANUSCRIPT

Yair, Y., Levin, Z., Tzivion, S., 1995. Lightning generation in a Jovian thundercloud: Results from an axisymmetric numerical cloud model. Icarus 115 (2), 421.

Yair, Y., Takahashi, Y., Yaniv, R., Ebert, U., Goto, Y., Sep. 2009. A study of the possibility of sprites in the atmospheres of other planets. J. Geophys. Res. (Planets) 114, 9002.

Yair, Y., 2012. New results on planetary lightning. Advances in Space Research 50 (3), 293.

Yoon, J., Song, M., Han, J., Hwang, S., Chang, W., Lee, B., Itikawa, Y., 2008. Cross sections for electron collisions with hydrogen molecules. Journal of Physical and Chemical Reference Data 37, 913. Itikawa database, www.lxcat.net, retrieved on October 23, 2013.

ACCEPTED MANUSCRIPT

ACCEPTED MANUSCRIPT

Appendix A

The 32 species included in the global kinetic model

Species

$H_2(X^1\Sigma^+_g, v = 0)$, He, H

H_2 ($B^1\Sigma^+_u$, $c^3\Pi_u$, $a^3\Sigma^+_g$, $C^1\Pi_u$, $d^3\Pi_u$)

H_2 ($X^1\Sigma^+_g$ (v = 1, … , 9))

H(2s ^{2}S), H(2p ^{2}P), H(3), H(4), H(5)

He ($2s^2$ ^{3}S), He_2 ($a\ ^3\Sigma_u^+$)

e^-, H^-

H^+, H_2^+, H_3^+, H_e^+, He_2^+, HeH^+

Appendix B

Reactions and rate coefficients associated with the electron driven kinetics and heavy particle chemistry. The rata coefficients for the electron-impact processes are evaluated using the calculated electron energy distribution function (EEDF) and the corresponding

ACCEPTED MANUSCRIPT

cross sections. When cross sections are not available, the rates of electronic processes are given as $k_e = a \times T_e^b \times exp(-c/T_e)$ where T_e (in eV) is the "electron temperature". The rate coefficients for the kinetic mechanisms involving heavy particles (neutrals and ions) are parameterized as $k_h = d \times (T_g/300)^e \times exp(-f/T_g)$ with T_g (in K) being the ambient gas temperature. The units of $k_{e,h}$ are $cm^3\ s^{-1}$ and $cm^6\ s^{-1}$ for two- and three-body reactions, respectively. The units of a and d are $cm^3\ s^{-1}$ (two body reactions) or $cm^6\ s^{-1}$ (three body reactions); b and e are non-dimensional parameters, and the units of c and f are eV and Kelvin (K), respectively. For radiative processes, the magnitudes A (s^{-1}), λ (nm) and κ stand for the Einstein coefficient of spontaneous radiative de-excitation, emission wavelength and optical thickness ($0 \le \kappa \le 1$) assumed. The reference sources of the cross sections and/or rates used are indicated in the last column of each of the tables below. The initials CS that appears in the tables below stand for cross section.

	Reaction	Reference
EEDF-dependent processes		
1	$He(1s^2\,^1S) + e \leftrightarrow He(2s^2\,^3S) + e$	[1]
2	$He(1s^2\,^1S) + e \rightarrow He^+ + 2\,e$	[1]
3	$H_2(X^1\Sigma^+_g) + e \rightarrow H_2(B^1\Sigma^+_u) + e$	[2]
4	$H_2(X^1\Sigma^+_g) + e \rightarrow H_2(c^3\Pi_u) + e$	[2]
5	$H_2(X^1\Sigma^+_g) + e \rightarrow H_2(a^3\Sigma^+_g) + e$	[2]
6	$H_2(X^1\Sigma^+_g) + e \rightarrow H_2(C^1\Pi_u) + e$	[2]

ACCEPTED MANUSCRIPT

7	$H_2(X^1\Sigma^+_g) + e \rightarrow H_2(d^3\Pi_u) + e$	[2]
8	$H_2(X^1\Sigma^+_g) + e \rightarrow H(1s\ ^2S) + H(1s\ ^2S) + e$	[2]
9	$H_2(X^1\Sigma^+_g) + e \rightarrow H(2s\ ^2S) + H(1s\ ^2S) + e$	[2]
10	$H_2(X^1\Sigma^+_g) + e \rightarrow H(2p\ ^2P) + H(1s\ ^2S) + e$	[2]
11	$H_2(X^1\Sigma^+_g) + e \rightarrow H(3) + H(1s\ ^2S) + e$	[2]
12	$H_2(X^1\Sigma^+_g) + e \rightarrow H(4) + H(1s\ ^2S) + e$	[3a]
13	$H_2(X^1\Sigma^+_g) + e \rightarrow H(5) + H(1s\ ^2S) + e$	[3a]
14	$H_2(X^1\Sigma^+_g) + e \rightarrow H_2^+ + 2\,e$	[2]
15	$H_2(B^1\Sigma^+_u) + e \rightarrow H_2^+ + 2\,e$	Same CS as used in reaction (14)
16	$H_2(c^3\Pi_u) + e \rightarrow H_2^+ + 2\,e$	Same CS as used in reaction (14)
17	$H_2(a^3\Sigma^+_g) + e \rightarrow H_2^+ + 2\,e$	Same CS as used in reaction (14)
18	$H_2(C^1\Pi_u) + e \rightarrow H_2^+ + 2\,e$	Same CS as used in reaction (14)
19	$H_2(d^3\Pi_u) + e \rightarrow H_2^+ + 2\,e$	Same CS as used in reaction (14)
20	$H_2(X^1\Sigma^+_g, v = 0) + e \leftrightarrow H_2(X^1\Sigma^+_g, v = 1) + e$	[2]
21	$H_2(X^1\Sigma^+_g, v = 0) + e \leftrightarrow H_2(X^1\Sigma^+_g, v = 2) + e$	[2]
22	$H_2(X^1\Sigma^+_g, v = 0) + e \leftrightarrow H_2(X^1\Sigma^+_g, v = 3) + e$	[2]

ACCEPTED MANUSCRIPT

23	$H_2(X^1\Sigma^+_g, v = 1) + e \leftrightarrow H_2(X^1\Sigma^+_g, v = 2) + e$	Same CS as used in reaction (20)
24	$H_2(X^1\Sigma^+_g, v = 2) + e \leftrightarrow H_2(X^1\Sigma^+_g, v = 3) + e$	Same CS as used in reaction (20)
25	$H_2(X^1\Sigma^+_g, v = 3) + e \leftrightarrow H_2(X^1\Sigma^+_g, v = 4) + e$	Same CS as used in reaction (20)
26	$H_2(X^1\Sigma^+_g, v = 4) + e \leftrightarrow H_2(X^1\Sigma^+_g, v = 5) + e$	Same CS as used in reaction (20)
27	$H_2(X^1\Sigma^+_g, v = 5) + e \leftrightarrow H_2(X^1\Sigma^+_g, v = 6) + e$	Same CS as used in reaction (20)
28	$H_2(X^1\Sigma^+_g, v = 6) + e \leftrightarrow H_2(X^1\Sigma^+_g, v = 7) + e$	Same CS as used in reaction (20)
29	$H_2(X^1\Sigma^+_g, v = 7) + e \leftrightarrow H_2(X^1\Sigma^+_g, v = 8) + e$	Same CS as used in reaction (20)
30	$H_2(X^1\Sigma^+_g, v = 8) + e \leftrightarrow H_2(X^1\Sigma^+_g, v = 9) + e$	Same CS as used in reaction (20)
31	$e + H(1s\ ^2S) \rightarrow H(2s\ ^2S) + e$	[3b]
32	$e + H(1s\ ^2S) \rightarrow H(2p\ ^2P) + e$	[3b]
33	$e + H(1s\ ^2S) \rightarrow H(3) + e$	[3b]
34	$e + H(1s\ ^2S) \rightarrow H(4) + e$	[3b]
35	$e + H(1s\ ^2S) \rightarrow H(5) + e$	[3b]
36	$H_2(X^1\Sigma^+_g, v = 0) + e \rightarrow H + H^-$	[4a] with CS fit of [4b]
37	$H_2(X^1\Sigma^+_g, v = 1) + e \rightarrow H + H^-$	[4a] with CS fit of [4b]

ACCEPTED MANUSCRIPT

38	$H_2(X^1\Sigma^+_g, v = 2) + e \rightarrow H + H^-$	[4a] with CS fit of [4b]
39	$H_2(X^1\Sigma^+_g, v = 3) + e \rightarrow H + H^-$	[4a] with CS fit of [4b]
40	$H_2(X^1\Sigma^+_g, v = 4) + e \rightarrow H + H^-$	[4a] with CS fit of [4b]
41	$H_2(X^1\Sigma^+_g, v = 5) + e \rightarrow H + H^-$	[4a] with CS fit of [4b]
42	$H_2(X^1\Sigma^+_g, v = 6) + e \rightarrow H + H^-$	[4a] with CS fit of [4b]
43	$H_2(X^1\Sigma^+_g, v = 7) + e \rightarrow H + H^-$	[4a] with CS fit of [4b]
44	$H_2(X^1\Sigma^+_g, v = 8) + e \rightarrow H + H^-$	[4a] with CS fit of [4b]
45	$H_2(X^1\Sigma^+_g, v = 9) + e \rightarrow H + H^-$	[4a] with CS fit of [4b]
46	$e + H(1s\ ^2S) \rightarrow H^+ + e + e$	[5]
47	$e + H(2s\ ^2S) \rightarrow H^+ + e + e$	Same CS as used in reaction (46)
48	$e + H(2p\ ^2P) \rightarrow H^+ + e + e$	Same CS as used in reaction (46)

Reaction	a	b	c	References
Te-dependent processes: ionization				

ACCEPTED MANUSCRIPT

49	$e + He_2^* \rightarrow He_2^+ + e + e$	9.75e-10	0.71	3.4	[6]
Te-dependent processes: dissociation					
50	$e + H_2 \rightarrow H + H + e$	1.7527e-7	-1.2366	12.5924	[7]
51	$e + H_2+ \rightarrow H+ + H + e$	1.0702e-7	0.04876	9.69028	[7]
52	$e + H_2+ \rightarrow H+ + H+ + 2\,e$	2.1202e-9	0.31394	23.2988	[7]
53	$e + H_3+ \rightarrow H_2+ + H + e$	4.8462e-7	-0.04975	19.1656	[7]
54	$e + He_2(a\,^3\Sigma_u^+) \rightarrow e + He + He$	3.8e-9			[6]
Te-dependent processes: attachment and dissociative attachment					
55	$e + H \rightarrow H^-$	3.46e-16	0.5		[6]
56	$e + H_2^+ \rightarrow H^+ + H^-$	2.17e-10	-0.2	0.2	[6]
Te-dependent processes: excitation/de-excitation					
57	$e + H(2s\,^2S) \rightarrow H(2p\,^2P) + e$	6.e-5			[8]
58	$e + H(2p\,^2P) \rightarrow H(2s\,^2S) + e$	2.e-5			[8]
59	$e + H(2s\,^2S) \rightarrow e + H(3)$	1.68e-6	0.1013	1.9	[6]
60	$e + H(2p\,^2P) \rightarrow e + H(3)$	1.68e-6	0.1013	1.9	[6]
Te-dependent processes: detachment					
61	$e + H- \rightarrow e + e + H$	2.32e-8	2.0	0.13	[6]
Te-dependent processes: recombination and dissociative recombination					
62	$e + H_2+ \rightarrow H + H(3)$	5.33e-8	-0.4		[9]
63	$e + H_2+ \rightarrow H + H(2s\,^2S)$	0.21e-8	-0.4		[9]

ACCEPTED MANUSCRIPT

ACCEPTED MANUSCRIPT

64	$e + H_3^+ \rightarrow H + H + H$	0.75e-8	-0.8		[9]
65	$e + H_3^+ \rightarrow H_2 + H$	0.75e-8	-0.8		[9]
66	$e + He_2^+ \rightarrow He(2s^2\,^3S) + He$	5.38e-11	-1		[10]
67	$e + He^+ \rightarrow He(2s^2\,^3S)$	6.76e-13	-0.5		[6]
68	$2\,e + He^+ \rightarrow He(2s^2\,^3S) + e$	1.31e-28	-4.4		[6]
69	$e + He^+ + He \rightarrow He(2s^2\,^3S) + He$	1.15e-30	-2.0		[6]
70	$2\,e + He_2^+ \rightarrow He(2s^2\,^3S) + He + e$	2.80e-20			[6]
71	$2\,e + He_2^+ \rightarrow He_2(a\,^3\Sigma_u^+) + e$	1.20e-21			[6]
72	$e + He_2^+ + He \rightarrow He(2s^2\,^3S) + 2\,He$	3.50e-27			[6]
73	$e + He_2^+ + He \rightarrow He_2(a\,^3\Sigma_u^+) + He$	1.50e-27			[6]
74	$e + HeH^+ \rightarrow H + He$	1.10e-9	-0.6		[6]
75	$e + H^+ \rightarrow H$	2.62e-13	-0.5		[6]
76	$2\,e + H^+ \rightarrow e + H$	8.8e-27	-4.5		[6]
77	$e + H_3^+ \rightarrow e + H^+ + 2\,H$	1.8e-8	0.95	10.5	[6]

Reaction		d	e	f	References
Heavy particle chemistry: ground neutrals					
78	$2\,H \rightarrow H_2$	6.04e-33	-1		[6]

ACCEPTED MANUSCRIPT

79	$2\,H + He \rightarrow H_2 + He$	5.80e-33	-1	[6]
80	$3\,H \rightarrow H + H_2$	6.00e-31	-1	[6]
81	$2\,H + H_2 \rightarrow 2\,H_2$	8.10e-33	-0.6	[6]

Heavy particle chemistry: electronically excited neutrals including Penning ionization

82	$H_2(d^3\Pi_u) + H_2 \rightarrow H_2(a^3\Sigma^+_g) + H_2$	1.2e-9		[11]
83	$H_2(a^3\Sigma^+_g) + H_2 \rightarrow H_2 + H_2$	1.7e-10		[11]
84	$He(2s^2\,^3S) + 2\,He \rightarrow He_2(a\,^3\Sigma_u^+) + He$	2.00e-34		[6]
85	$He_2(a\,^3\Sigma_u^+) + H_2 \rightarrow 2\,He + H_2$	1.50e-15		[6]
86	$He(2s^2\,^3S) + H_2 \rightarrow H(2p\,^2P) + H + He$	1.40e-11		[6]
87	$He + H(3) \rightarrow H + He$	1.00e-11		[6]
88	$H(2p\,^2P) + H_2 \rightarrow 3\,H$	2.1e-11		[6]
89	$H(2s\,^2S) + H_2 \rightarrow 3\,H$	2.1e-11		[6]
90	$H(3) + H_2 \rightarrow H + H_2$	2.0e-9		[6]
91	$He(2s^2\,^3S) + He(2s^2\,^3S) \rightarrow He + He^+ + e$	8.7e-10	0.5	[6]
92	$He(2s^2\,^3S) + He(2s^2\,^3S) \rightarrow He_2^+ + e$	2.03e-9	0.5	[6]
93	$He(2s^2\,^3S) + He_2(a\,^3\Sigma_u^+) \rightarrow He^+ + 2\,He + e$	5.0e-10		[6]
94	$He(2s^2\,^3S) + He_2(a\,^3\Sigma_u^+) \rightarrow He_2^+ + He + e$	2.0e-9		[6]
95	$He(2s^2\,^3S) + H \rightarrow H^+ + He + e$	1.1e-9		[6]

ACCEPTED MANUSCRIPT

96	$He(2s^2\,^3S) + H_2 \rightarrow H_2^+ + He + e$	2.9e-11	[6]
97	$He(2s^2\,^3S) + H_2 \rightarrow H + HeH^+ + e$	3.0e-12	[6]
98	$2\,He_2(a\,^3\Sigma_u^+) \rightarrow He^+ + 3\,He + e$	3.0e-10	[6]
99	$2\,He_2(a\,^3\Sigma_u^+) \rightarrow He_2^+ + 2\,He + e$	1.2e-9	[6]
100	$He_2(a\,^3\Sigma_u^+) + H \rightarrow 2\,He + H^+ + e$	2.2e-10	[6]
101	$He_2(a\,^3\Sigma_u^+) + H_2 \rightarrow H_2^+ + 2\,He + e$	2.2e-10	[6]

Heavy particle chemistry: vibrational-vibrational processes

102	$H_2(v = 1) + H_2(v = 1) \rightarrow H_2(v = 2) + H_2$	9.3e-15	[12]
103	$H_2(v = 1) + H_2(v = 2) \rightarrow H_2(v = 3) + H_2$	1.7e-14	[12]
104	$H_2(v = 1) + H_2(v = 3) \rightarrow H_2(v = 4) + H_2$	2.6e-14	[12]
105	$H_2(v = 1) + H_2(v = 4) \rightarrow H_2(v = 5) + H_2$	3.3e-14	[12]
106	$H_2(v = 1) + H_2(v = 5) \rightarrow H_2(v = 6) + H_2$	3.2e-14	[12]
107	$H_2(v = 1) + H_2(v = 6) \rightarrow H_2(v = 7) + H_2$	2.5e-14	[12]
108	$H_2(v = 1) + H_2(v = 7) \rightarrow H_2(v = 8) + H_2$	1.6e-14	[12]
109	$H_2(v = 1) + H_2(v = 8) \rightarrow H_2(v = 9) + H_2$	9.5e-15	[12]

Heavy particle chemistry: vibrational-translational processes

110	$H_2(v = 1) + H_2 \rightarrow H_2 + H_2$	1.6e-16	[12]
111	$H_2(v = 2) + H_2 \rightarrow H_2(v = 1) + H_2$	7.8e-16	[12]

ACCEPTED MANUSCRIPT

112	$H_2(v = 3) + H_2 \rightarrow H_2(v = 2) + H_2$	3.0e-15		[12]
113	$H_2(v = 4) + H_2 \rightarrow H_2(v = 3) + H_2$	1.0e-14		[12]
114	$H_2(v = 5) + H_2 \rightarrow H_2(v = 4) + H_2$	3.2e-14		[12]
115	$H_2(v = 6) + H_2 \rightarrow H_2(v = 5) + H_2$	1.0e-13		[12]
116	$H_2(v = 7) + H_2 \rightarrow H_2(v = 6) + H_2$	3.3e-13		[12]
117	$H_2(v = 8) + H_2 \rightarrow H_2(v = 7) + H_2$	1.1e-12		[12]
118	$H_2(v = 9) + H_2 \rightarrow H_2(v = 8) + H_2$	3.3e-12		[12]
Ionic chemistry: ion-ion recombination				
119	$H^- + H^+ \rightarrow H + H$	3.900e-07		[13]
120	$He^+ + H^- \rightarrow H + He$	2.3e-7	-0.5	[6]
121	$HeH^+ + H^- \rightarrow H_2 + He$	1.0e-7		[6]
122	$He_2^+ + H^- \rightarrow H + 2\,He$	1.0e-7		[6]
123	$H^+ + H^- \rightarrow H(2s\ ^2S) + H$	9.0e-11	0.83	[6]
124	$H^+ + H^- \rightarrow H(2p\ ^2P) + H$	9.0e-11	0.83	[6]
125	$H^+ + H^- \rightarrow H(3) + H$	1.8e-7	-0.5	[6]
126	$H_2^+ + H^- \rightarrow H + H_2$	2.0e-7	-0.5	[6]
127	$H_3^+ + H^- \rightarrow 2\,H_2$	2.0e-7	-0.5	[6]
Ionic chemistry: positive ions				
128	$H^+ + H_2 \rightarrow H_2^+ + H$	1.19e-22		[7]

ACCEPTED MANUSCRIPT

129	$H_2^+ + H \rightarrow H^+ + H_2$	6.4e-10		[6]
130	$H_2^+ + H_2 \rightarrow H_3^+ + H$	2.0e-9		[14]
131	$He^+ + 2\,He \rightarrow He_2^+ + He$	1.4e-31	-0.6	[10]
132	$He^+ + H \rightarrow H^+ + He$	1.9e-15		[6]
133	$He^+ + H \rightarrow HeH^+$	1.58e-15	-0.3	[6]
134	$He^+ + H_2 \rightarrow H^+ + H + He$	3.7e-14		[6]
135	$He^+ + H_2 \rightarrow H_2^+ + He$	7.2e-15		[6]
136	$HeH^+ + H \rightarrow H_2^+ + He$	9.1e-10		[6]
137	$HeH^+ + H_2 \rightarrow H_3^+ + He$	1.5e-9		[6]
138	$He_2^+ + H \rightarrow H^+ + 2\,He$	3.5e-10		[6]
139	$He_2^+ + H_2 \rightarrow HeH^+ + H + He$	1.76e-10		[6]
140	$H^+ + He \rightarrow HeH^+$	8.4e-19	-4.5	[6]
141	$H^+ + H + H_2 \rightarrow H_2^+ + H_2$	1.0e-34		[6]
142	$H^+ + H_2 + He \rightarrow H_3^+ + He$	1.5e-29		[6]
143	$H_2^+ + He \rightarrow HeH^+ + H$	1.3e-10		[6]
Ionic chemistry: negative ions				
144	$H^- + H \rightarrow H_2 + e$	1.800e-9		[14]
145	$H^- + He \rightarrow He + H + e$	8.e-12	0.5	[6]

ACCEPTED MANUSCRIPT

ACCEPTED MANUSCRIPT

	Reaction	A (s^{-1})	λ (nm)	κ	References
	Radiative processes				
146	$H(2p\ ^2P) \rightarrow H + h\nu$	4.69e+8	121.56	1	[15]
147	$H(3) \rightarrow H + h\nu$	5.57e+7	102.57	1	[15]
148	$H(4) \rightarrow H + h\nu$	1.27e+7	79.25	1	[15]
149	$H(5) \rightarrow H + h\nu$	4.12e+8	94.97	1	[15]
150	$H(3) \rightarrow H(2s\ ^2S) + h\nu$	2.24e+7	656.27	1	[15]
151	$H(3) \rightarrow H(2p\ ^2P) + h\nu$	6.31e+6	656.28	1	[15]
152	$H(4) \rightarrow H(2s\ ^2S) + h\nu$	9.66e+6	486.13	1	[15]
153	$H(4) \rightarrow H(2p\ ^2P) + h\nu$	2.57e+6	486.13	1	[15]
154	$H(5) \rightarrow H(2s\ ^2S) + h\nu$	4.95e+6	434.04	1	[15]
155	$H(5) \rightarrow H(2p\ ^2P) + h\nu$	9.42e+6	434.04	1	[15]
156	$H(4) \rightarrow H(3) + h\nu$	8.98e+6	1875.10	1	[15]
157	$H(5) \rightarrow H(3) + h\nu$	2.20e+6	1281.81	1	[15]
158	$H(5) \rightarrow H(4) + h\nu$	2.70e+6	4051.20	1	[15]
159	$H_2(d^3\Pi_u) \rightarrow H_2(a^3\Sigma^+_g) + h\nu$	3.33e+7	612.00	1	[11]

ACCEPTED MANUSCRIPT

160	$H_2(a^3\Sigma^+_g) \rightarrow H + H + h\nu$	8.77e+7	400.00	1	[11]

[1] Helium IST-Lisbon electron impact cross section database in LxCat at www.lxcat.laplace.univ-tlse-fr

[2] H_2 Phelps electron impact cross section database in LxCat at www.lxcat.laplace.univ-tlse-fr

[3a] H_2 IST-Lisbon electron impact cross section database in LxCat at www.lxcat.laplace.univ-tlse-fr

[3b] H IST-Lisbon electron impact cross section database in LxCat at www.lxcat.laplace.univ-tlse-fr

[4a] Bardsley J. N., Wadehra J. M., 1979, *Physical Review A*, **20**, 1398.

[4b] Celiberto R., Janev R. K., Laricchiuta A., Capitelli M., Wadehra J. M., Atems D. E., *Atomic Data and Nuclear Tables,* **77** (2), 161-213 (2001).

[5] I.Bray's electron impact cross section database at http://atom.curtin.edu.au/CCC-WWW/

[6] Liu D. X., Bruggeman P., Iza, F. Rong M. Z., Kong M. G., 2010, *Plasma Sources Science and Technology,* **19**, 025018.

[7] Méndez I., Gordillo-Vázquez F.J., Herrero V., Tanarro I., 2006, *Journal of Physical Chemistry A*, **110**, 6060.

ACCEPTED MANUSCRIPT

ACCEPTED MANUSCRIPT

[8] Seaton M. J. 1955, *Proc. Phys. Soc. (London),* **68**, 457.

[9] Mitchell J. B. A., 1990, *Physics Reports,* **186**, 216.

[10] Alves L. L., Gousset G., Ferreira C. M., 1992, *J. Phys. D: Appl. Phys.* **25**, 1713.

[11] Bretagne J., Godart J., Puech V., 1981, *J. Phys. B: At. Mol. Phys.* **14**, L761.

[12] Capitelli M., Celiberto R., Cacciatore M., 1994, *Advances in Atomic, Molecular, and Optical Physics* **33**, 321.

[13] Fridman A., 2008, *Plasma Chemistry* (Cambridge University Press)

[14] Capitelli M., Ferreira C. M., Gordiets B. F., Osipov A. I., 2000, *Plasma Kinetics in Atmospheric Gases* (Berlin, Springer).

[15] Wiese W. L., Smith M. W., Glennon B. M., 1966, *Atomic Transition Probabilities, vol 1*, (Washington DC, NSRDS-NBS 4).

ACCEPTED MANUSCRIPT

ACCEPTED MANUSCRIPT

Appendix C

In this appendix, we show that the total amount of electrons liberated and photons produced during the Maxwell relaxation of an atmospheric volume is independent of the initial electron density if the external electric field varies slowly in time during the screening process. This is a generalization of the argument exposed in (Li et al. 2007) where it was applied to the calculation of ionization in a streamer head. Although this result may appear counter-intuitive, its underlying reason is that when the initial electron density is higher, the faster relaxation exactly compensates the increased frequency of impact ionization or excitation.

Under the assumption that the externally applied field varies slowly and the geometry is close to planar, a local field undergoes Maxwell relaxation and decays exponentially following equation (7) in section 5, with $E_p = 0$:

$$\frac{dE}{dt} = -\frac{\sigma}{\epsilon_0} E = -\frac{e\mu_e N_e}{\epsilon_0} E. \tag{C1}$$

Now consider any two-body process involving electrons and an abundant species. The most important cases are ionization:

$$e + H_2 \rightarrow 2e + H_2^+, \tag{C2}$$

and impact excitation,

$$e + H_2 \rightarrow e + H_2^*. \tag{C3}$$

These processes can be described by equations of the form

ACCEPTED MANUSCRIPT

$$\frac{dN_X}{dt} = \nu(E/N)N_e, \tag{C4}$$

where N_X is the density of the species that we are interested in, like N_e for ionization or the density of H_2^- or H_2^*. Dividing (C4) by (C1) we see that the N_e on the right hand sides cancel and the variables E and N_X can be separated:

$$\frac{dN_X}{dE} = -\frac{\epsilon_0 \nu}{e\mu_e E}. \tag{C5}$$

This can be integrated to yield

$$N_X(t) - N_X(0) = -\frac{\epsilon_0}{e}\int_{E(0)}^{E(t)} \frac{\nu dE}{\mu_e E}. \tag{C6}$$

After a long time, the electric field is fully relaxed ($E(t) \rightarrow 0$) and the increase in N_X is independent on the initial electron density.

ACCEPTED MANUSCRIPT

- One dimensional model of the impact of lightning on lower ionosphere of Saturn.
- The onset of the field cannot be assumed immediate, induction field is included.
- A threshold field proposed for rapid electron growth in a conducting atmosphere.
- Faint halos and sprites appear if ionosphere's base is at 1000 km above 1 bar.
- Chemical fingerprint and optical emissions are modelled with a detailed kinetic model.

ACCEPTED MANUSCRIPT